



# Lewis acid catalysis of polydopamine electropolymerisation as a tool for shaping its morphology and electrochemical properties

Krzysztof Polaczek<sup>1,2</sup>, Adrian Olejnik<sup>1,3,\*</sup> , Justyna Gumieniak<sup>4</sup>, Agnieszka Kramek<sup>4</sup>, Jakub Karczewski<sup>5</sup>, and Katarzyna Siuzdak<sup>1</sup>

<sup>1</sup> Centre for Plasma and Laser Engineering, The Szewalski Institute of Fluid-Flow Machinery, Polish Academy of Sciences, Fiszerza 14 St, 80-231 Gdańsk, Poland

<sup>2</sup> Department of Biomedical Chemistry, Faculty of Chemistry, University of Gdańsk, Wita Stwosza 63 St, 80-308 Gdańsk, Poland

<sup>3</sup> Department of Metrology and Optoelectronics, Faculty of Electronics, Telecommunications and Informatics, Gdańsk University of Technology, Narutowicza 11/12 St, 80-233 Gdańsk, Poland

<sup>4</sup> The Faculty of Mechanics and Technology, Rzeszów University of Technology, Kwiatkowskiego 4 Street, 37-450 Stalowa, Wola, Poland

<sup>5</sup> Institute of Nanotechnology and Materials Engineering and Advanced Materials Center, Gdańsk University of Technology, Narutowicza 11/12, 80-233 Gdańsk, Poland

**Received:** 10 February 2024

**Accepted:** 29 April 2024

© The Author(s), 2024

## ABSTRACT

Organic–inorganic semiconductor interfaces are of utmost importance in many photoelectrochemical applications, including water splitting and photodegradation of pollutants. The current work focuses on the fabrication and characterisation of transition metal-loaded polydopamine (PDA) electropolymerised on the surface of titania nanotubes. The structural studies via X-ray photoelectron spectroscopy and electron microscopy confirmed the catalytic effect of d-metal salts on the formation of the PDA layer during electropolymerisation. Cu and Ni loading leads to a significant enhancement of the visible absorption compared to that of the pristine PDA, also confirmed by the density functional theory calculations. Although the boost is greater for the thickest coatings, an excess amount of polymer suppresses the charge transfer and thus photocurrent generation. Synthesis in acidic conditions—optimal for photosensitisation—provides structures with a strong increase in the photocurrent quantum efficiency in the visible range, equal to 20% at 400 nm.

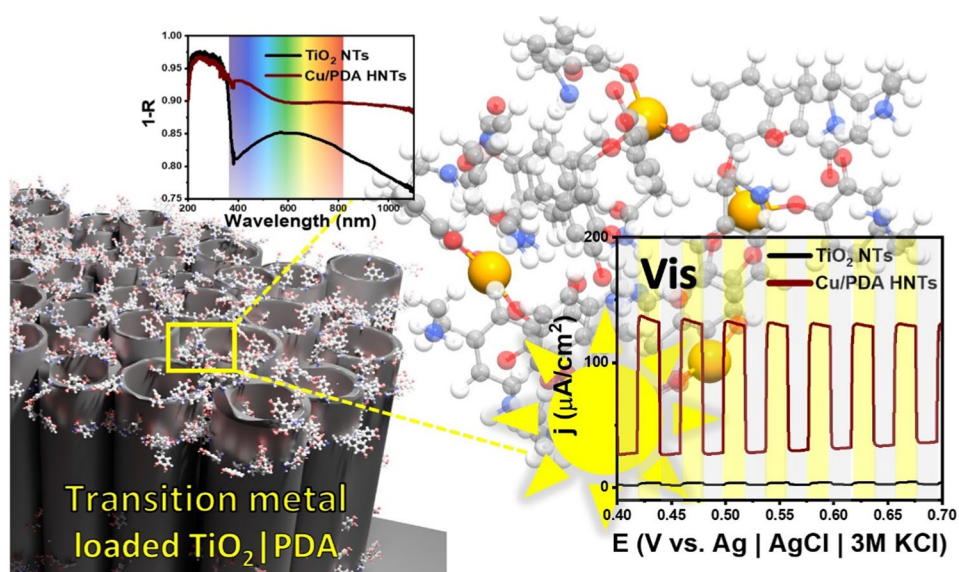
Handling Editor: Pedro Camargo.

Address correspondence to E-mail: aolejnik@imp.gda.pl

<https://doi.org/10.1007/s10853-024-09722-1>

Published online: 16 May 2024

## GRAPHICAL ABSTRACT



## Introduction

Polydopamine (PDA) is a bioinspired melanin-like polymer formed by the oxidative polymerisation of dopamine [1]. It can be obtained via several synthesis protocols. In the most general approach, the reaction of PDA formation occurs in an alkaline environment ( $\text{pH} > 7.5$ ), during which dopamine is oxidised with oxygen from the air [2]. The alkaline pH during PDA formation is crucial for the Michael addition reaction to occur, which is important for further polymer formation [3, 4]. This is followed by mutual autopolymerisation of reduced and oxidised monomer molecules, leading to a polymer film with a variety of structures [5]. The presence of catechol groups on the surface of PDA is associated with high adhesion to all types of materials, both organic and inorganic [6]. This allows PDA to be used in numerous processes for coating a variety of materials [3, 7, 8]. However, high adhesion is not the only interesting property of polydopamine, as it is also characterised by high biocompatibility [2], a complex mechanism of electrical conductivity [9] and the ability to absorb light in both the ultraviolet, visible and IR light ranges [10]. In addition, PDA can be easily obtained by an electropolymerisation reaction. This process, compared to oxidative polymerisation methods, not only produces a more homogeneous and thicker polymer layer but also reduces the time consumed to prepare the samples [1, 11]. Given

the properties mentioned above, PDA has important applications as, e.g. photodegradation of pollutants [6], absorption of heavy metals, dyes and pathogens [3], drug delivery [2], membranes for oil/water separation [12], elements of composites for energy storage [13], or as nanomaterials for Zn battery electrodes [14]."

The presence of catechol functional groups in the PDA structure also enables the formation of coordination bonds with metal ions, transition metal ions included [15]. The ability to form this type of bonds has also been used for the binding of heavy metals by PDA [6, 16]. However, these are not the only examples of the use of metal-PDA bonding. Wang et al. used a PDA layer as a matrix to deposit copper ions. The resulting material was able to catalytically remove dyes from aqueous solutions [17]. Similar Cu/PDA complexes were also used by Xu et al. to modify the surface of hydrogels. The copper ions thus delivered exhibited antimicrobial properties [18]. Li et al., in turn, used PDA and its adhesive properties as well as its ability to form coordination bonds with metals to synthesise Cu and Ni nanoparticles [15]. The addition of d-block metal ions also has a significant effect on the polymer formation reaction itself. This is because transition metal ions such as Lewis acids are catalysts for the Michael addition reaction [19]. Both salts and complex compounds of metals such as Cu, Ni, Fe, Co and Cr have been used for this purpose [20,

21]. Overall, PDA can be considered as a matrix for the metal loading similar to the metal organic frameworks, where metal ions are also coordinated by the organic compounds. Such an approach can be beneficial in energy storage as components of supercapacitors and batteries [22–24].

Transition metal salts have also been used in PDA synthesis. Zhang et al. reported that the addition of  $\text{CuSO}_4/\text{H}_2\text{O}_2$  leads to faster polymer deposition [25]. Yang et al. also indicated the catalytic effect of transition metals on PDA deposition, with the difference that they used Ni, Co, and Mn salts. The use of such catalysts also made it possible to incorporate  $\text{Ni}^{2+}$  ions into the PDA structure [26].

“Titania-based materials such as titanium dioxide nanotubes (TNT) are thoroughly studied n-type semiconductor materials that can be easily fabricated with desired geometries via, e.g. anodisation. Unfortunately, due to the large band gap (3.2 eV), radiation absorption by  $\text{TiO}_2$  is mainly limited to the ultraviolet light range [27, 28]. Applications of titania-based materials range from photodetectors [29], antifouling [30]—due to its high hydrophilicity, light-driven reactions [31], in particular water splitting [32, 33]—typically with dopants, and separation processes [12]—as a component of a membrane.”

The presence of metals itself is important, from the point of view of improving the photoactivity of the  $\text{TiO}_2$  NTs. Numerous sources in the literature describe metal doping or decoration with metal nanoparticles, leading to enhancement the photoelectrochemical and photocatalytic activity of semiconductors [34–37]. An example of such modifications is the doping of  $\text{TiO}_2$  nanotubes with chromium, which led to an increase in the recorded photocurrent [35, 38]. A similar phenomenon has been observed with doping with copper [39] and nickel [40].

Semiconductive inorganic–organic interfaces with the ability of photocurrent generation have a broad scope of photoelectrochemical and photovoltaic applications. Among them, photoelectrocatalysis of water splitting [41, 42], photodegradation of pollutants [43, 44], and photoelectrochemical synthesis [45] are of utmost importance in various subfields of engineering and environmental sciences. These processes are based on the light absorption by the semiconductor electrode leading to the formation of excited electrons. Then, in the electric field of the space-charge region on

the semiconductor–liquid interface, a separation of the electron–hole pairs occurs, so that they can be transported towards the contacts and drive the reaction in the liquid. Inorganic–organic interfaces can lead to enhanced optical absorption and separation, thus they are important in practical applications. Those catalytic processes require both strong visible light absorption and fast charge transfer to speed up the desired reaction, and preferably cheap, scalable and sustainable production [46]. Such a feature is a marker of efficient photosensitisation and can be useful, e.g. in (photo) electrochemical sensing and degradation, where the same material can be used for both purposes [47]. Therefore, exploration of new synthetic routes for semiconductor modifications is relevant.

Quantum chemistry methods such as density functional theory (DFT) can be helpful tools to explain experimentally observed phenomena in electrochemical studies. Specifically, interaction energies between molecules [48] or surfaces [49] can be estimated to understand adsorption and bond formation. Density of states analyses [48, 50] can be helpful for elucidation of effect of dopant on the electronic structure and the band gap.

In the previous work [51], we reported the superior enhancement of photocurrent generation in TNT\_PDA heterostructures caused by changes introduced in the electronic structure. We also observed a parallel change in the electrochemical response to the redox marker, i.e. after PDA modification, an oxidation peak emerged.

In the abovementioned framework, the main goal of the paper is to show the possibilities of modifying  $\text{TiO}_2$  nanotubes with electropolymerised PDA with embedded transition metal ions: Cu, Ni and Cr. The main source of this research motivation is that incorporating such metals would further enhance the reversibility of the redox marker reaction, imposing faster charge transfer. To the authors' best knowledge, such composites are investigated for the first time. Exploration of the synthesis parameter space shows the significant influence of both the metal type and electropolymerisation pH on the structure and photoelectrochemical properties. Moreover, DFT calculations strongly support the experimental result that the visible absorption is enhanced in the case of Cu and Ni loading, while it is suppressed in the case of Cr. Finally, reactive molecular dynamics simulations of the complexation dynamics suggest catalytic activity of copper salts to the PDA growth via Lewis acid catalysis.

## Experimental

Sections devoted to the reagents used in experiments, details of the anodisation, computational details and basic theory behind DFT calculations are given in SI file.

### Hydrogenation of nanotubes and electropolymerisation of dopamine in the presence of transition-metal ions

Because bare titania is an n-type semiconductor and exhibits low conductivity, electrodeposition of the conducting polymer is hampered. Therefore, we applied the electrochemical hydrogenation method to change the electric properties, allowing polymer deposition [52].

Hydrogenation was carried out in a two-electrode system with the TNT sample as the cathode and a platinum net as the anode. The reaction was carried out for three minutes in the solution containing  $1 \times$  Tris buffer in 0.5 M sodium sulphate and a voltage of 5 V between the electrodes.

The polydopamine film on the HNTs surface was prepared 20 min after electrochemical hydrogenation (during this time, the sample was immersed in a 0.5 M  $\text{Na}_2\text{SO}_4$  solution) using the cyclic voltammetry method. The process was realised in a three-electrode system with HNTs as the working electrode, a platinum net as the counter electrode, and  $\text{Ag}|\text{AgCl}||3 \text{ M KCl}$  as the reference electrode. This

setup is preserved throughout the study. Electropolymerisation experiments were carried out potentiodynamically, and 50 cycles of cyclic voltammetry were recorded with a 20 mV/s scan rate at the potential range from  $-0.5$  to  $+1.0$  V using a BioLogic SP-150 potentiostat–galvanostat. The solution contained of 5 mM of dopamine hydrochloride and 25 mM of different transition metals salts:  $\text{Cu}(\text{NO}_3)_2 \cdot 3\text{H}_2\text{O}$ ,  $\text{Cu}(\text{CH}_3\text{COO})_2 \cdot \text{H}_2\text{O}$ ,  $\text{CuSO}_4$ ,  $\text{Ni}(\text{NO}_3)_2 \cdot 6\text{H}_2\text{O}$ ,  $\text{Ni}(\text{CH}_3\text{COO})_2 \cdot 4\text{H}_2\text{O}$ ,  $\text{Cr}(\text{NO}_3)_3 \cdot 9\text{H}_2\text{O}$  dissolved in  $1 \times$  Tris–0.5 M  $\text{Na}_2\text{SO}_4$  (10: 90% v/v) and deaerated with Argon for 20 min before starting the deposition. Considering the metal ion that was present in the electrolyte and its pH, the samples were labelled according to the information provided in Table 1. The following labelling was proposed for the obtained samples:

The pH value (below 7.5) of the prepared solutions was the innate/default value obtained as a result of adding different transition metal salts to the  $1 \times$  Tris: 0.5 M  $\text{Na}_2\text{SO}_4$  solution. The reaction carried out at pH 7.5 was based on the previous experience of our group, which showed the highest photocurrent and high conductivity of the obtained polydopamine layer for those electropolymerisation conditions [36]. For those solutions, the pH value was established by adding 1 M NaOH and controlled by a pH meter (EZDO portable pH meter MP-103). For the preparation of the reference sample, an electropolymerisation reaction was carried out in a 0.5 M  $\text{Na}_2\text{SO}_4$  solution consisting of  $1 \times$  Tris buffer and 5 mM dopamine (pH 7.5) without transition metal salts.

**Table 1** Set of samples obtained after dopamine polymerisation was carried out in the presence of different transition metal ion precursors and using hydrogenated titania nanotubes as a substrate

pH	Precursor					
	$\text{Cu}(\text{NO}_3)_2 \cdot 3\text{H}_2\text{O}$	$\text{Cu}(\text{CH}_3\text{COO})_2 \cdot \text{H}_2\text{O}$	$\text{CuSO}_4$	$\text{Ni}(\text{NO}_3)_2 \cdot 6\text{H}_2\text{O}$	$\text{Ni}(\text{CH}_3\text{COO})_2 \cdot 4\text{H}_2\text{O}$	$\text{Cr}(\text{NO}_3)_3 \cdot 9\text{H}_2\text{O}$
4.2						Cr/PDA <sub>4,2</sub> HNTs
5.5			Cu/PDA <sub>5,5</sub> HNTs			Cr/PDA <sub>5,5</sub> HNTs
5.9				Ni/PDA <sub>5,9</sub> HNTs		
6.5		Cu/PDA <sub>6,5</sub> HNTs				
6.7					Ni/PDA <sub>6,7</sub> HNTs	
7.5	Cu/PDA <sub>7,5</sub> HNTs			Ni/PDA <sub>7,5</sub> HNTs		Cr/PDA <sub>7,5</sub> HNTs

Me/PDA<sub>pH</sub>HNTs

where Me—types of metal ions precursor presented during the electropolymerisation reaction, PDA—polydopamine layer, pH—value during the reaction, and HNTs—layer of hydrogenated titanium dioxide nanotubes.

## Characteristics of structure, morphology and optical properties

The surface morphology of the electrodes was investigated by means of a Quanta FEG 250 (FEI) Schottky field-emission scanning electron microscope (SEM) equipped with a secondary ET electron detector with a beam accelerating voltage of 10 kV.

UV–Vis spectra were registered using a PerkinElmer Lambda 35 dual-beam spectrophotometer in reflectance mode in the range of 200–1100 nm and a scanning speed of 120 nm/min. The integration sphere was used to collect the light scattered from the sample during illumination and to obtain diffuse reflectance  $R$ . Reflective mode was used due to the non-transparency of the samples. Optical properties are presented as  $1-R$  in the main paper, in contrast to Kubelka–Munk [53], a representation of which can be found in the SI file (Fig. S12).

Raman spectra were collected using a confocal micro-Raman spectrometer (InVia Renishaw) with sample excitation by an argon ion laser emitting at 514 nm and operating at 10% of its total power. Spectra were recorded in the wavelength range from 100 to 3200  $\text{cm}^{-1}$  with a 1-s sample exposure and 3 accumulations for each measurement. For each sample, Raman spectra were recorded in two different areas and presented as the average of the measurements.

X-ray photoelectron spectroscopy (XPS) measurements were taken using a Thermo Scientific™ K-Alpha™ X-ray Photoelectron Spectrometer. The samples were irradiated with low-energy X-ray radiation ( $\text{Al K}\alpha = 1486.7 \text{ eV}$ ). Measurements were taken under a pressure of  $10^{-9}$  to  $10^{-8}$  mbar. Survey spectra were registered using a pass energy of 150 eV and a step size of 1 eV. The equipment was calibrated using  $\text{C1s}$  (284.5 eV). In turn, high-resolution spectra were recorded in the oxygen  $\text{O 1s}$ , titanium  $\text{Ti 2p}$ , and carbon  $\text{C 1s}$  binding energy ranges using a pass energy of 20 eV and step size of 0.1 eV.

## Electrochemical and photoelectrochemical characterisation

Cyclic voltammetry (CV) measurements were taken using a BioLogic SP-150 potentiostat–galvanostat in a three-electrode system with the prepared NTs sample as the working electrode (area =  $1 \text{ cm}^2$ ), a platinum net as the counter electrode and  $\text{Ag|AgCl|3 M KCl}$

as the reference electrode. Measurements were taken in a 5 mM solution of potassium ferrocyanide and potassium ferricyanide in potassium chloride 1 M (pH 7.0) in the potential range of  $-0.5 \text{ V}$  to  $+1.0 \text{ V}$  with a scan rate of 20 mV/s.

Photoelectrochemical measurements were taken using an Autolab PGSTAT 302N potentiostat–galvanostat in a three-electrode system with the prepared sample as the working electrode (area =  $1 \text{ cm}^2$ ), a platinum net as the counter electrode and  $\text{Ag|AgCl|3 M KCl}$  as the reference electrode. The prepared samples were tested in a 0.5 M  $\text{Na}_2\text{SO}_4$  (pH 7) solution in an electrochemical cell with a high transmittance quartz window that allowed sample irradiation within the full UV–Vis range. Before the electrochemical measurements, the electrolyte was deaerated using Argon (5.0), and then during the measurements, the flow of Argon was maintained above the electrolyte to avoid introducing oxygen to the system. The measurement was started with 5 cycles of cyclic voltammetry in the potential range of  $-0.4 \text{ V}$  to  $+0.8 \text{ V}$  with a scan rate of 50 mV/s. Then the sample was illuminated by a solar light simulator (XE lamp 150W, LOT-Oriel) for 3 min. The irradiation intensity was set to  $100 \text{ mW cm}^{-2}$  and the calibration was carried out using a silicon solar cell (Rera). The optical system was equipped with an AM 1.5 air mass filter and an additional optical filter (GG-420 Shott). Photocurrents were measured via two linear voltammetry scans in the potential range of  $-0.4 \text{ V}$  to  $0.8 \text{ V}$ , with a scan rate of 10 mV/s. During the first measurement, photocurrents were registered in the presence of visible light, while during the second measurement route, the samples were exposed to the whole light spectrum generated by the xenon lamp. Sample irradiation was controlled by an automated shutter with 1 s light and dark periods. Both electrochemical measurements and the operation of the shutter were controlled by the dedicated software associated with Autolab (Nova).

The stability of the samples was measured by performing 100 subsequent voltammetry cycles (BioLogic SP-150 potentiostat–galvanostat) in a three-electrode system with the prepared sample as the working electrode (geometrical area =  $1 \text{ cm}^2$ ), a platinum net as the counter electrode and  $\text{Ag|AgCl|3 M KCl}$  as the reference electrode. The experiments were carried out in 0.5 M  $\text{Na}_2\text{SO}_4$  in the potential range of  $-0.5 \text{ V}$  to  $+1.0 \text{ V}$  with a scan rate of 20 mV/s.

## Incident photocurrent conversion efficiency (IPCE)

Quantum efficiency maps were measured with a photoelectric spectrometer designed for quantum efficiency measurements (Instytut Fotonowy, Poland) equipped with a monochromator. All IPCE measurements were taken in a 0.5 M Na<sub>2</sub>SO<sub>4</sub> solution with the prepared samples as the working electrode, a platinum counter electrode and Ag|AgCl|3 M KCl as the reference electrode. The wavelength range was set from 200 to 550 nm with a 25 nm step and the potential range between 0 and 800 mV with a 200 mV step. Therefore, as a result, the map was plotted against the applied potential and wavelength. The illumination source was calibrated with a Xe lamp using the silicon reference cell.

Monochromator with two diffraction gratings and maximum efficiencies at 300 nm and 500 nm is applied in IPCE spectrometer. The highest possible output light power density equals to 4 mW cm<sup>-3</sup> nm<sup>-1</sup>, which corresponds to 10–50 μW cm<sup>-2</sup> light intensities reaching the sample mounted in the cuvette. Wavelength ranges available are between 200 and 1200 nm with resolution on the level of 1 nm. In the presented work, this range was narrowed to 200–600 nm due to negligible photocurrent produced by the samples during illumination above 600 nm. It is understandable also because to generate photocurrent from such photons, the sample should have had less than 2 eV band gap.

## ReaxFF calculations of the complexation

The molecular structures of the PDA and its units were built in the tool provided by Atomistix ToolKit QuantumWise (ATK, Synopsys, USA), as reported in [54]. Density functional theory (DFT) computations were used to calculate density of states (DOS) spectra for the metal-complexed PDA molecules to investigate the influence of the complexation on the electronic structure. Moreover, ReaxFF molecular dynamics (MD) simulations of the crosslinking were performed for pristine PDA and Cu-loaded PDA according to the NVT Nose–Hoover method. The system consisted of 16 PDA dopaminechrome units placed inside a simulation box of 3 nm × 3 nm × 3 nm with periodic boundary conditions. The time step for the ReaxFF MD simulations was equal to 0.5 fs, with the total time of the simulation being equal to 1 ns with 3 elements of the Noose-Hoover chain, a 300 K thermostat temperature

and a 50 fs thermostat timescale. MD trajectories were analysed via radial distribution functions (RDF), nearest neighbour, void-size distribution, mass distribution and coordination number evolution methods implemented in the Quantum ATK package.

## Results and discussion

### Electropolymerisation of dopamine in presence of transition metal ions

The deposition of the metal-loaded PDA on hydrogenated titania nanotubes was performed via several CV in the solution containing dopamine and metal ions. The main purpose of using electropolymerisation instead of standard oxygen-induced self-polymerisation is the uniformity of the coating. Justification of this issue is given in Fig. S1, which compares the SEM images of the loosely spaced titania nanotubes covered with electropolymerised PDA (upper row) and self-polymerisation (lower row). In the former case, the PDA covers both the inner and outer walls of the nanotubes having several nm thickness, which is roughly uniform for the whole set of tubes. The cross-sectional view depicts some aggregations on the surface, although they constitute only a minor part of the image. In the latter case, the PDA resides mostly at the bottom of the sample, filling the space between the tubes. Almost all the surface is cluttered by the PDA aggregates and the approach to most of the tubes is blocked by the non-uniform layer. Another argument supporting the choice of electropolymerisation is the controllability of the thickness using the number of CV cycles, which was shown in our previous work [51]. Although this is also possible in the standard self-polymerisation approach, especially for less porous surfaces, or even titania nanotubes [55], it could not be straightforwardly replicated at nanotube substrates in our cases (see the SEM figures).

CV curves registered during PDA electropolymerisation in the presence of Cu (II) ions are shown in Fig. 1a–c. For clarity, the second, and every tenth cycle have been placed on the graph. The red curve corresponding to the analogous pristine PDA polymerisation is given for comparison. During electropolymerisation of pure dopamine, CV curves exhibit an anodic peak at +0.6 V (D<sub>O</sub>) and cathodic peak at +0.1 V (D<sub>R</sub>), attributed to the redox couple of dopamine/dopamine quinone [1]. The shape of the

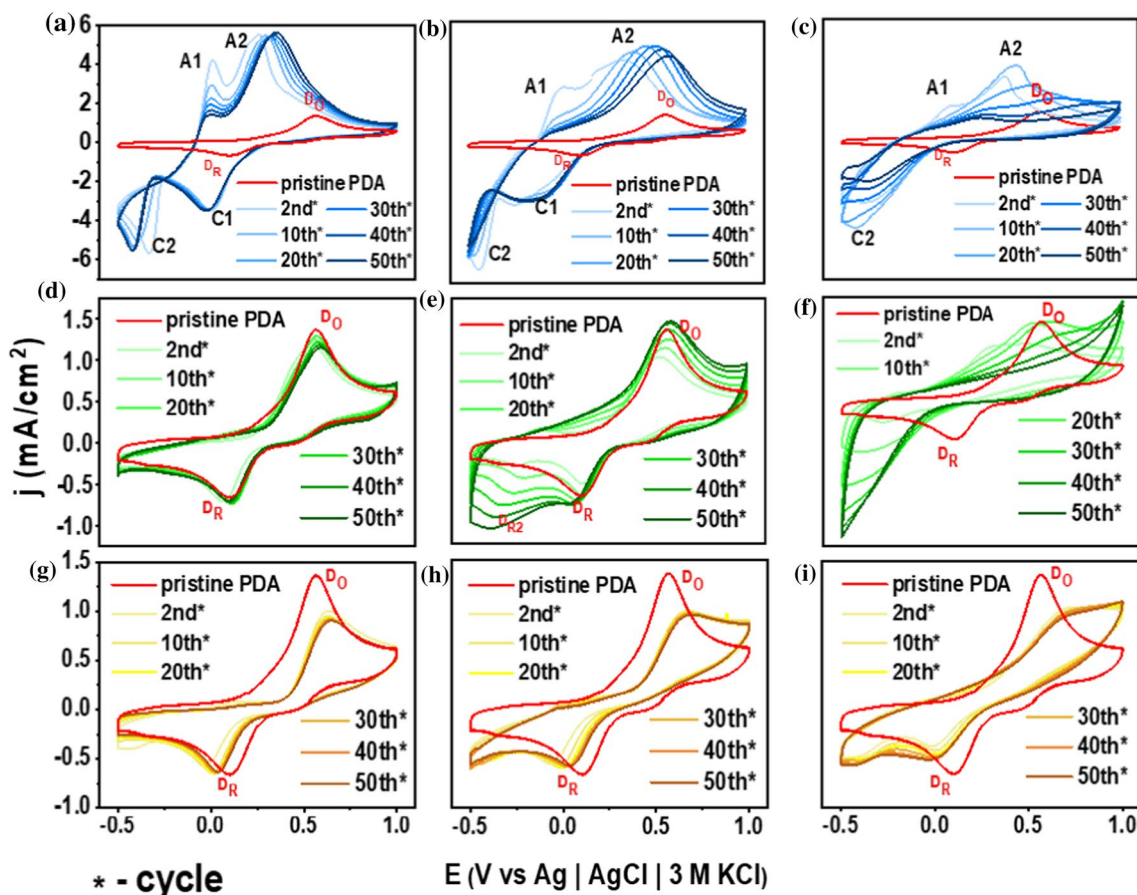


**Figure 1** Selected curves of the polydopamine electrodeposition reaction in the presence of:  $\text{Cu}^{2+}$  ions (25 mM) (blue plots) performed at different pHs (a) 5.5 ( $\text{Cu/PDA}_{5.5}\text{HNTs}$ ), (b) 6.5 ( $\text{Cu/PDA}_{6.5}\text{HNTs}$ ), (c) 7.5 ( $\text{Cu/PDA}_{7.5}\text{HNTs}$ );  $\text{Ni}^{2+}$  ions (25 mM) (green plots) performed at different pHs (d) 5.9 ( $\text{Ni/PDA}_{5.9}\text{HNTs}$ ), (e) 6.7 ( $\text{Ni/PDA}_{6.7}\text{HNTs}$ ), (f) 7.5

( $\text{Ni/PDA}_{7.5}\text{HNTs}$ );  $\text{Cr}^{3+}$  ions (25 mM) (yellow plots) performed at different pHs (g) 4.2 ( $\text{Cr/PDA}_{4.2}\text{HNTs}$ ), (h) 5.5 ( $\text{Cr/PDA}_{5.5}\text{HNTs}$ ), (i) 7.5 ( $\text{Cr/PDA}_{7.5}\text{HNTs}$ ) of monomer solution (dopamine concentration 5 mM). The CV curves (50 cycles) were recorded with a 20 mV/s scan rate.

recorded curves does not change throughout cycling in this reference case. However, the shape of the voltamperograms and the value of the recorded current changed substantially after introducing copper ions into the electrolyte. During the electropolymerisation at pH = 5.5 (Fig. 1a), two cathodic peaks emerged at potential values of 0.0 V and -0.4 V, corresponding to the reduction of copper ions:  $\text{Cu}^{2+} + e^- \rightarrow \text{Cu}^+$  (C1) and  $\text{Cu}^+ + e^- \rightarrow \text{Cu}$  (C2), respectively. When polarisation was carried out in the anodic direction, two oxidation peaks were found at potential values of 0.0 V and +0.3 V, originating from the reactions  $\text{Cu}^0 \rightarrow \text{Cu}^+ + e^-$  (A1) and  $\text{Cu}^+ \rightarrow \text{Cu}^{2+} + e^-$  (A2) [56]. The faradaic reactions resulting from the change in the copper oxidation state completely overshadowed the signals characteristic of dopamine during

its electrodeposition process. As the polymer film is growing, the shift of the oxidation peak from +0.3 to +0.4 V (Fig. 1 a (A2)) and the reduction peak from -0.3 V to -0.4 V (Fig. 1 a (A2)) can be observed. This behaviour suggests a decrease in the working electrode conductivity caused by the electrodeposition of the polymer [57] or copper complexes, which inhibits the charge transfer (described further in the XPS analysis) [58]. Comparing the loci of the peaks between the CV graphs shown in Fig. 1a–c, one can observe that the increase in the pH of the solution results in a shift of the oxidation peaks towards higher potential values and the reduction peaks towards lower potential values (Fig. 1b, c). Such behaviour strongly suggests a further reduction in the conductivity characteristic for the alkaline-based

PDA. A more alkaline solution also results in lower current values of the recorded oxidation and reduction peak, as well as faster current drops between successive CV cycles during the electropolymerisation process. The largest current decreases in the given pH range (Fig. 1a–c) were noted for the  $\text{Cu}^0$  to  $\text{Cu}^{+1}$  (A1) oxidation and for the  $\text{Cu}^{+2}$  to  $\text{Cu}^{+1}$  (C1) reduction peak. During electropolymerisation in  $\text{pH} = 7.5$  (Fig. 1c), the C1 cathodic peak disappeared, indicating that the  $\text{Cu}^{+1}$  oxidation state is stabilised, and metallic Cu is not restored with cycling.

When the electrodeposition was performed in the presence of nickel (II) ions, the shape of the CV curves was quite similar to those registered for the pristine PDA (Fig. 1d). Additionally, no significant changes in the current were observed during the reaction, suggesting a lesser amount of the deposited PDA in the acidic pH. With an increase of the pH value up to 6.7 (Fig. 1e), the peaks on the CV—characteristic to the PDA units redox couples—do not change their positions. However, during the formation of polymeric film, an increase in the current density was recorded across the whole potential range, both for the faradaic and capacitive components, which is related to the polymer deposition on the electrode surface and formation of the conductive film—contrary to the Cu case [59]. It may also be a consequence of coordination connections forming between PDA and Ni(II) ions in a different geometry or electronic alignment in comparison with the Cu-loaded PDA [60]. For a peak at a potential of +0.6 V ( $D_{\text{O}}$ ), an increase of oxidation currents can be observed. The same trend was noted for the reduction current at +0.1 V ( $D_{\text{R}}$ ). Apart from those changes, an increase in the current value was noted for the reduction peak at the potential of -0.4 V, ascribed to a reduction reaction of dopaminechrome to leukodopaminechrome (Fig. 1e ( $D_{\text{R}2}$ )) [1]. The increasing current for the reduction reaction suggests the catalytic influence of nickel ions on the formation of leukodopaminechrome [20]. Electropolymerisation at pH 7.5 (1 f) is also characterised by an initial increase in oxidation current at a potential of +0.5 V ( $D_{\text{O}}$ ). Then, after 10 cycles of electropolymerisation, a current decrease for this peak occurs. Similar to the curves recorded at pH 6.7, a visible reduction peak at -0.4 V (Fig. 1f ( $D_{\text{R}2}$ )) is also present. Moreover, it is characterised by a significant increase in the current for this range and shifts towards a lower potential, suggesting a plummeting

conductivity, analogously to the Cu case. In other words, the high pH of the PDA deposition led to hindered charge transfer, regardless of the metal influence (Fig. S2 and Table S1 and corresponding subsection in SI file).

In the third case, the electropolymerisation process was carried out in the presence of the chromium (III) ions. The shape of the recorded CV is similar to those recorded for electropolymerisation of pure dopamine, although the current magnitudes are notably reduced (Fig. 1 g, h, i). Moreover, the oxidation peak ( $D_{\text{O}}$ ) is shifted towards higher potential values (+0.5 V  $\rightarrow$  +0.6 V) and the reduction peak ( $D_{\text{R}}$ ) towards lower potential values (+0.1 V  $\rightarrow$  0.0 V), which is related to a slower charge transfer, inhibited even more for higher synthesis pH values. Moreover, with an increase in the solution pH used during electropolymerisation (Fig. 1i), the oxidation current at +1.0 V increases, which is described as either shifted oxidation of PDA units, or Cr(III) oxidation to higher oxidation states [60]. Similarly, the reduction current at -0.5 V presumably indicates Cr(III) ion reduction  $\text{Cr}^{3+} + \text{e}^- \rightarrow \text{Cr}^{2+}$  [61]. Comparing the electropolymerisation reaction in the presence of Cr(III) with those performed in the presence of other metal ions, there is a less intense current drop during subsequent cycles of electropolymerisation. Considering that the drop is the result of a decrease in the monomer concentration caused by polymer deposition near the electrode surface, the amount of the formed PDA is supposedly less than in other cases. Although characteristic peaks of dopamine oxidation ( $D_{\text{O}}$ ) and reduction ( $D_{\text{R}}$ ) are observed, the PDA layer is thinner than that obtained under other conditions, which is discussed in the following section.

Overall reproducibility of the electropolymerisation syntheses has been verified. CV curves from electropolymerisation of three samples for each metal modifications are presented in Fig. S3. In general, the shape is qualitatively the same in all cases. Minor differences include the spread of current magnitudes resulting from varying sample surface area and variable sample resistance. The latter can be noted for the sample 2 of the Cr modification. Uncertainty of the current originates from the uncertainty of the measurement of the area wettable by the electrolyte—there is intrinsic randomness there. Uncertainty of the resistance originates from the quality of the electrical contacts between the components of the composite material.



## Morphology of the modified nanotubes

The SEM images shown in Fig. 2 depict an aligned and highly ordered layer of titanium dioxide nanotubes, confirming the effectiveness and repeatability of the anodisation protocol. The bare nanotubes (Fig. 2a) developed an outer diameter of  $136.2 \pm 15$  nm and a length of  $4.9 \pm 0.46$   $\mu\text{m}$ . After modification, an increase in wall thickness is observed, which is due to the deposition of a polydopamine film on the tubular surface. The thickness of the obtained layer ( $t_{\text{PDA}}$ ) was estimated taking into account the diameter of the modified nanotubes ( $d_{\text{Me/PDApHHNTs}}$ ) and the diameter of the unmodified ones ( $d_{\text{NTs}}$ ) according to the following equation:

$$t_{\text{PDA}} = \frac{d_{\text{Me/PDApHHNTs}} - d_{\text{NTs}}}{2}$$

The thicknesses for the series of materials containing the PDA layer were calculated as averages of at least 100 points, and those values are provided in Table 2.

These results indicate that a higher pH favours the dopamine electropolymerisation reaction, resulting in a thicker polymer layer [62, 63]. This is particularly evident for samples fabricated at pH 7.5 in the presence of copper (Fig. 1d) and nickel (Fig. 1f) ions, suggesting that metal ions increase the stability of the PDA

**Table 2** Thicknesses of PDA film in the obtained samples

Sample label	Thickness of PDA layer [nm]
PDA <sub>7.5</sub> HNTs	$8.60 \pm 1.1$
Cu/PDA <sub>5.5</sub> HNTs	$7.21 \pm 2.7$
Cu/PDA <sub>6.5</sub> HNTs	$9.61 \pm 1.8$
Cu/PDA <sub>7.5</sub> HNTs	$11.53 \pm 4.6$
Ni/PDA <sub>5.9</sub> HNTs	$5.97 \pm 1.1$
Ni/PDA <sub>6.7</sub> HNTs	$10.42 \pm 3.9$
Ni/PDA <sub>7.5</sub> HNTs	$11.27 \pm 1.3$
Cr/PDA <sub>4.2</sub> HNTs	$3.36 \pm 1.0$
Cr/PDA <sub>5.5</sub> HNTs	$4.68 \pm 1.7$
Cr/PDA <sub>7.5</sub> HNTs	$8.89 \pm 2.1$

coating, e.g. through coordination bond crosslinking [64]. This is also in line with the fact that a thicker PDA hinders the charge transfer to a higher extent (Fig. S1). As the synthesis pH increases, so does the thickness, while the surface conductivity plummets. Importantly, the metal-loaded PDA layer is amorphous, as the XRD signals of the modified nanotubes are identical to the pristine ones (Fig. S4). Despite the crystallinity of titania is important for electrochemical applications [65], such an outcome is expected because of the small amount of the deposited material and the fact that the PDA—which is amorphous—is a dominant component of the coating. Furthermore, the

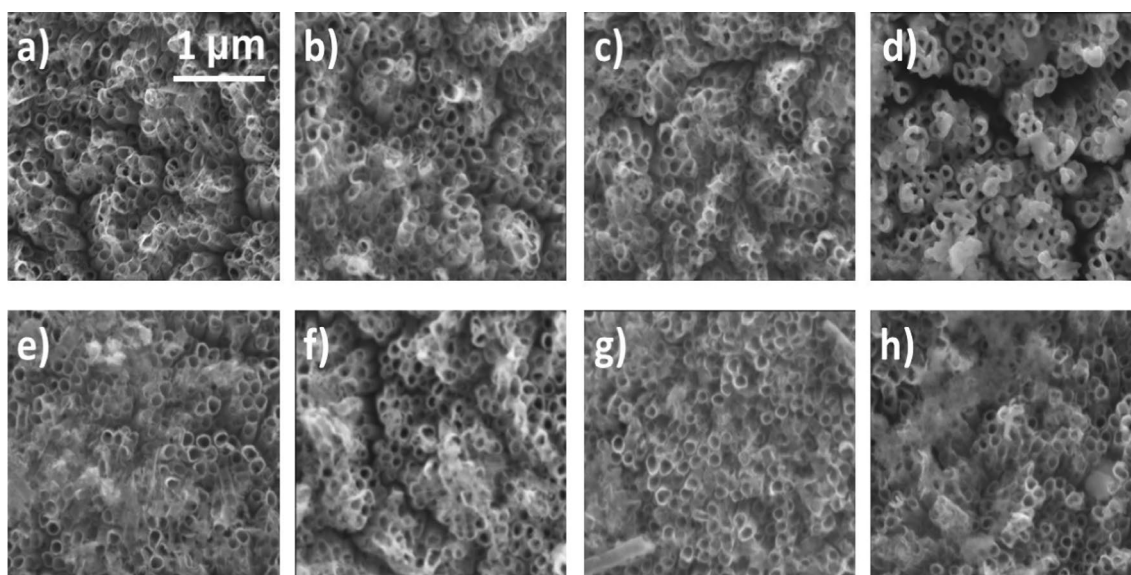


**Figure 2** SEM images of (a) bare nanotubes, (b) PDA<sub>7.5</sub>HNTs, (c) Cu/PDA<sub>5.5</sub>HNTs, (d) Cu/PDA<sub>7.5</sub>HNTs, (e) Ni/PDA<sub>5.9</sub>HNTs, (f) Ni/PDA<sub>7.5</sub>HNTs, (g) Cr/PDA<sub>4.2</sub>HNTs, (h) Cr/PDA<sub>7.5</sub>HNTs.

calculated thickness values are in agreement with the results obtained from the XPS analysis (and UV–Vis spectroscopy, illustrating strong structure–property relationships within the metal-loaded PDA.

The specific surface area of the electrodes has been estimated through a series of CV measurements with variable scan rates in 1 M KCl electrolyte in small electrochemical windows, where the response is primarily capacitive. The results and elaboration on the applied methodology are given in Fig. S5, S6, and Table S2. In general, the specific surface area is 10–30 times greater than the geometric area, which is reasonable considering SEM results. Cu-containing sample fabricated at the pH = 7.5 results in the highest area, while Ni samples tend to yield smallest. Overall, smaller synthesis pH leads to smaller total surface area, also in agreement with SEM inspections.

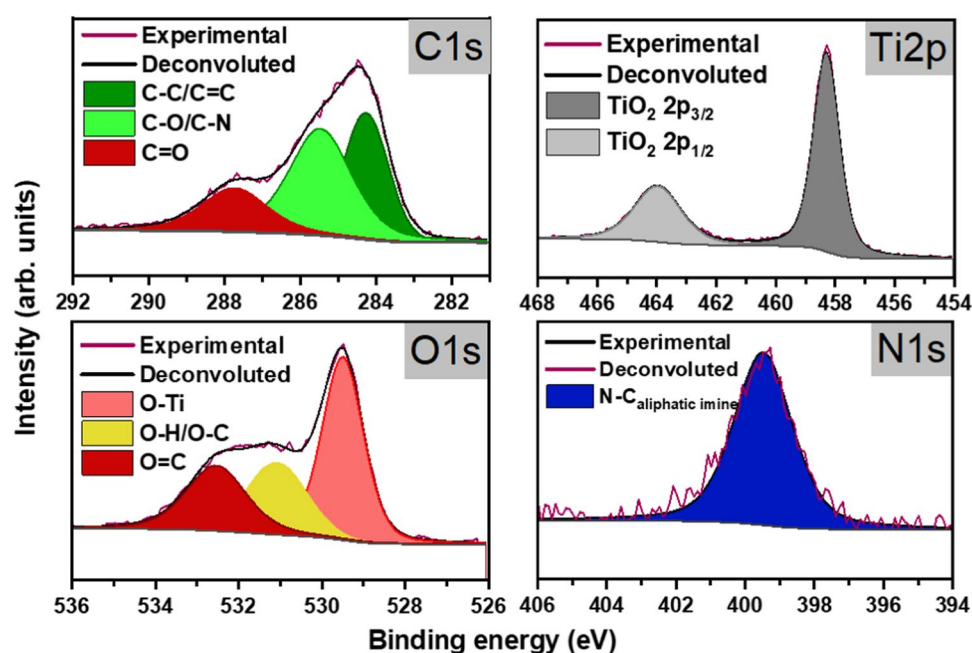
### X-ray photoelectron spectroscopy investigation of the PDA chemistry and transition metal valence states

An XPS analysis was performed to obtain information on the chemistry of titania and organic materials without and with embedded metal species. The high-resolution XPS spectrum for the reference PDA sample (Fig. 3) shows characteristic peaks for titanium and oxygen, as well as carbon and nitrogen, present exclusively in polydopamine. In the binding energy range typical for carbon, three peaks were

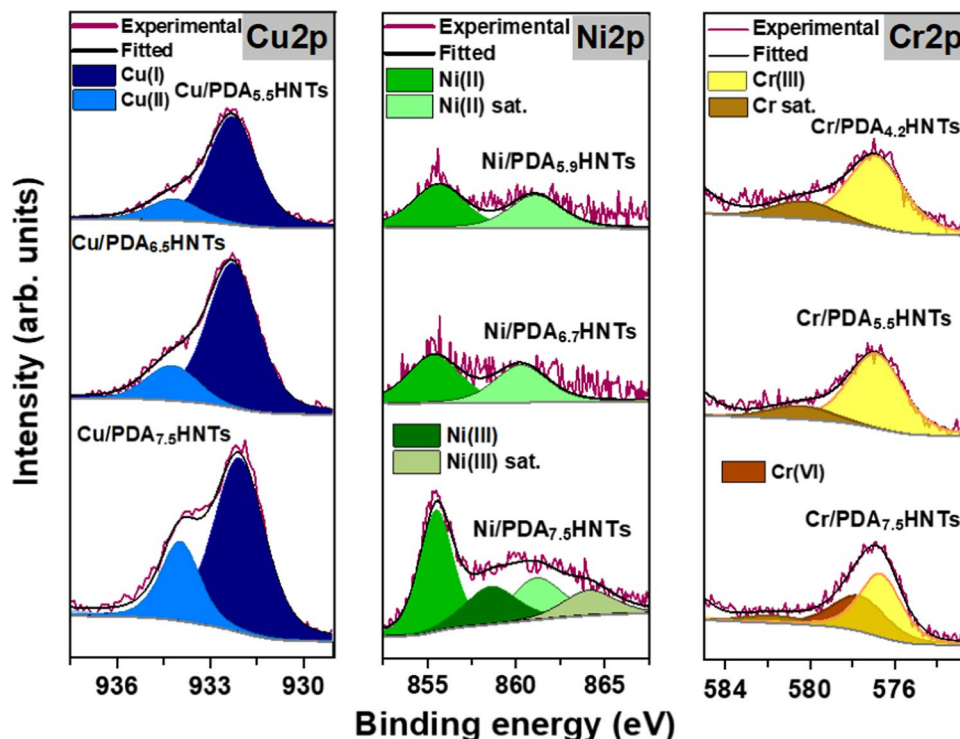
distinguished. They correspond to  $sp^2$  and  $sp^3$  carbon hybridisation: C = C and C–C (284 eV), single bonds between carbon and oxygen or nitrogen (285.7 eV), and the C = O double bond (287.7 eV). Such carbon species are present in a polymeric chain [66] and can be partially attributed to the carbon-containing species remaining after calcination and from the XPS instrument itself. The 1 s carbon spectrum of pure PDA is representative of all the inorganic/organic junctions obtained in the presence of different metal ions. Therefore, the chemical structure of the metal-loaded PDA carbon backbone is presumably unaltered by the metal and all the property changes result mostly from complexation. The share of individual carbon species for all the investigated samples is collected in Table S3. The nitrogen spectrum for the pure polydopamine represents N–C bonding (399 eV), characteristic of secondary amines [67]. The oxygen region was deconvoluted into three signals: one originating from the O–Ti bonding (529.5 eV) present in TiO<sub>2</sub> nanotubes, a peak (530.9 eV) associated with both O–H and quinone C = O catechol groups [66, 67], and the one attributed to O–C. The spectrum of Ti (see Fig. 3c) shows a doublet characteristic of TiO<sub>2</sub> without Ti<sup>3+</sup> signals [38].

Figure 4 presents the XPS spectra regions corresponding to the metals in the presence of which the dopamine electropolymerisation reaction was carried out. The copper spectrum (Fig. 4a, blue plots)

**Figure 3** High-resolution XPS spectra for reference PDA<sub>7.5</sub>HNTs sample recorded in the binding energy region characteristic for carbon, titanium, oxygen and nitrogen.



**Figure 4** High-resolution XPS spectra for binding energy spectrum of (a) Cu2p, (b) Ni2p and (c) Cr2p present in various titania/polydopamine heterojunctions.



shows the presence of this metal in two oxidation states in all prepared samples. The peak at 932.4 eV is described as the copper in the first oxidation state (metallic copper) [68], while the peak at 934 eV corresponds to copper (II) [68].

Samples prepared in the presence of nickel ions (4 b, green plots) at a lower pH contain nickel(II), as indicated by the peak at 855.5 eV [69]. However, when prepared at a higher pH, an additional peak appears at 858.5 eV, described as nickel(III) [70].

For the chromium-containing materials (Fig. 4c, yellow plots), a peak is visible for Cr(III) at the lower pH (576.8 eV), while at pH 7.5, an additional peak is observed at (577.6 eV), which is described as originating from  $\text{Cr}(\text{OH})_3$ , although some literature data suggest the presence of a peak from Cr(VI) at that position [71]. This indicates that at higher pHs, part of the precursor used during electropolymerisation can undergo further oxidation. However, the ratio of the area of the metal-derived peaks to the PDA-derived is similar for samples with the same metal, indicating that its increasing percentage content is a result of the increasing thickness of the polymer layer. An exception is observed for samples prepared with the addition of acetates (both copper and nickel), where the percentage of metals is lower compared to the case when other precursors were applied. This is due to the

lower solubility of acetates in water [72]. However, the lower availability of metal ions does not affect the thickness of the polymer layer, which grows with the increasing pH for all precursors used. This indicates that the presence of metal ions—as a Lewis acid—has catalytic properties on the ongoing Michael addition reaction and the formation of the PDA layer, regardless of its solubility or dissociation [21]. Additionally, an increase in the pH of the solution promotes the oxidation of metals, as evidenced by the increased proportion of more oxidised forms, such as copper: 0.51% for pH 5.5 and 0.99% for pH 7.5 [73]. It can also affect the appearance of more oxidised forms, such as Ni(III).

Due to the presence of numerous peaks from PDA in the oxygen region and the ambiguity of the fitting procedure (Fig. 5a–b), it is challenging to determine precisely the types of compounds formed by the metals on this basis. Thus, the XPS spectra resolved at each metal characteristic region (Fig. 4) remain the only key to access the information on the oxidation state of metals embedded into the PDA.

The nitrogen spectrum for the reference  $\text{PDA}_{7.5}\text{HNTs}$  sample shown in Fig. 3 is representative of those recorded for the copper samples, where one peak is present corresponding to N–C bonds derived from the aliphatic imine. For the  $\text{Ni}/\text{PDA}_{6.9}\text{HNTs}$  (Fig. 5d) as well as the  $\text{Ni}/\text{PDA}_{7.5}\text{HNTs}$  sample (not

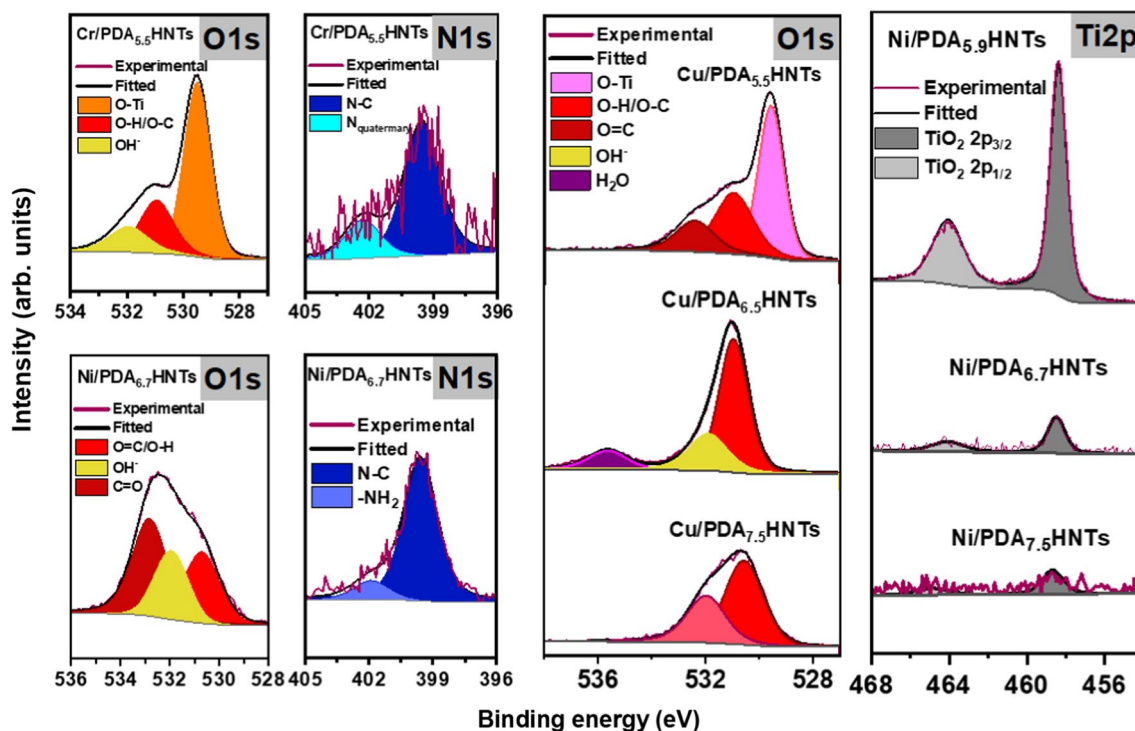


**Figure 5** High-resolution XPS spectra of characteristic PDA elements for Me/PDA<sub>pH</sub>HNTs sample. Spectra were recorded in the binding energy range typical of oxygen, nitrogen and titanium.

shown), the N1s spectrum shows the presence of two peaks. The first (399 eV) corresponds to the already-described N–C bonds, while the second with the maxima at 402 eV originates from the primary amine group [57]. In the spectrum for Cr/PDA<sub>5.5</sub>HNTs (Fig. 5c), a peak at 401 eV indicates the presence of one corresponding to the quaternary amino group [74], whose presence may be due to the formation of chromium(III) PDA coordination bonds reported for various Schiff base compounds [75, 76].

In Fig. 5e, the oxygen part of the XPS spectrums for different Cu/PDAHNTs junctions is presented. For the Cu/PDA<sub>5.5</sub>HNTs materials, the spectrum exhibits peaks matching the pure polydopamine film. With the increase of the electrolyte's pH, i.e. for Cu/PDA<sub>6.5</sub>HNTs and Cu/PDA<sub>7.5</sub>HNTs, an additional peak appears at 531.9 eV, corresponding to OH<sup>-</sup> groups derived from the metal hydroxide, and its area further increases with the increasing pH [39, 77]. This signal is also visible in the oxygen spectra deconvoluted for the Ni- (Fig. 5b) and Cr-containing (Fig. 5a) samples. However, those peaks can be attributed to the O–C bond, but shifted towards lower binding energies resulting from the

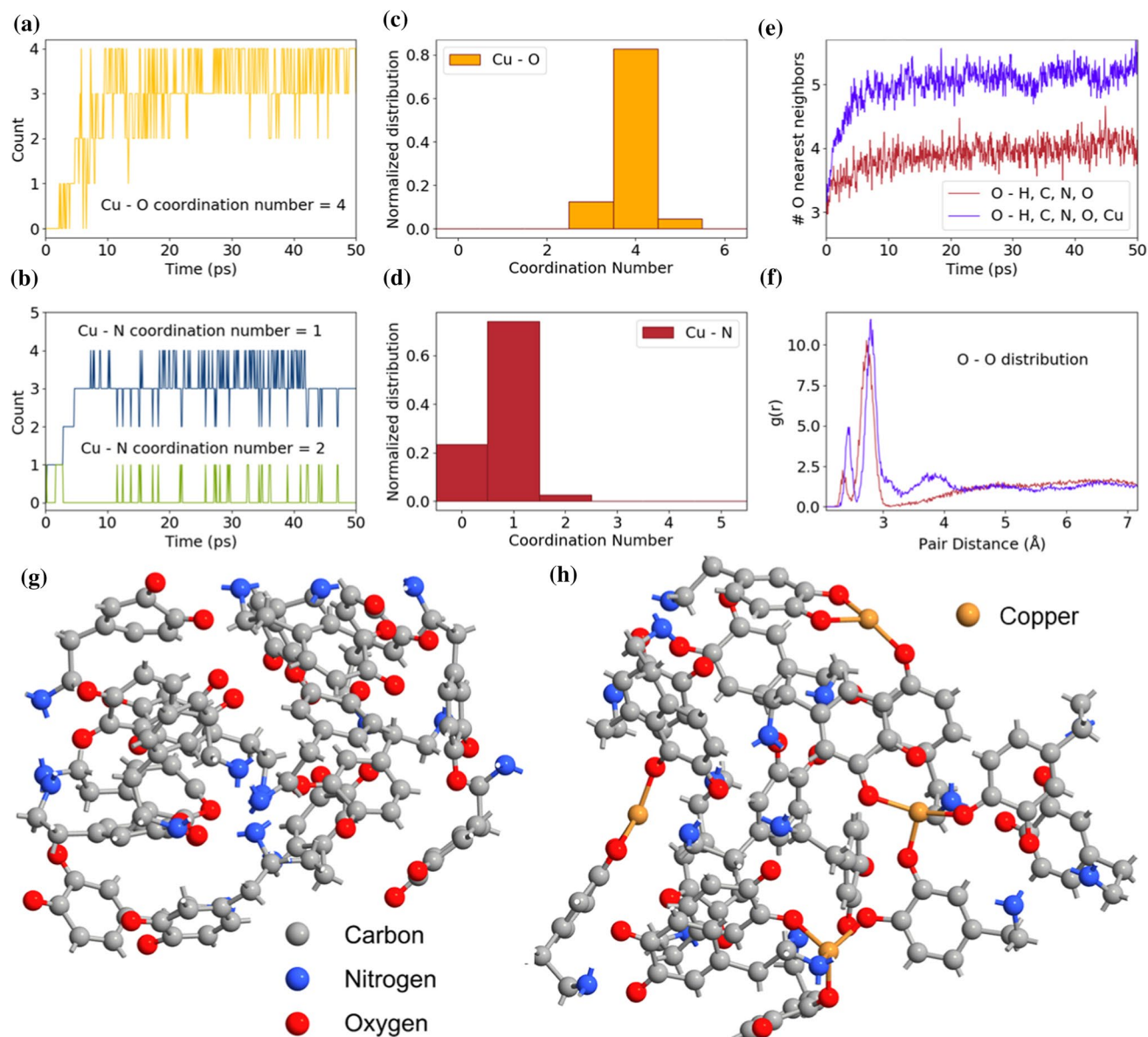
formation of a coordination bond between the metal and the dopamine unit [26]. On the Cu/PDA<sub>6.5</sub>HNTs O1s spectrum, a peak at 535.6 eV most presumably corresponds to a NaKLL signal from Na salt in the electrolyte taken during electropolymerisation [78] or absorbed water [79].

Figure 5f shows the changes in the intensity of the titanium doublet for three Ni/PDA junctions depending on the synthesis conditions. Since XPS provided information about the material from its surface region (several monolayers) [80], the decreased intensity for Ti is associated with an increased thickness of the PDA layer covering the nanotube surfaces. In general, as the pH during electropolymerisation increases, so does the PDA thickness. A similar effect is observed when other metal ions were present in the electrolyte, which is further consistent with the results of the SEM analysis (see Table 2 in the Morphology section). The changes in the percentage contribution of individual elements are shown in Table S1. An increase in the carbon and metallic content with the pH during electropolymerisation is noted and has significant consequences for the optical and photoelectrochemical properties.

## ReaxFF molecular dynamics of the PDA complexation

An attempt to reproduce the complexation dynamics of the PDA by the Cu(I/II) cations was performed via ReaxFF MD (Fig. 6). PDA loaded with Cu cation was chosen due to its largest propensity for the

photosensitisation described in further sections. In general, 16 single-ringed monomers were put into a simulation box with 4 Cu atoms and an NVT protocol was carried out for 1 ns at a temperature of 300 K. The majority of changes occur during the first 50 ps of the simulation; therefore, trajectory analysis is presented for this short period.



**Figure 6** Analysis of the molecular dynamics trajectory of the Cu complexation by the PDA units; (a–b) time evolution of the Cu coordinated with 4 O atoms (yellow), with a single N atom (navy blue) and 2 N atoms (green); (c–d) distribution of the Cu–O (yellow) and Cu–N (red) coordination numbers at the final stage of the trajectory; (e) time evolution of the O atoms’ nearest

neighbours with 3 Ang cutoff for the Cu-complexed PDA (blue) and pristine PDA (dark red); (f) radial distribution function of the O–O interactions for the complexed (blue) and pristine PDA (dark red); (g–h) last frame of the 1 ns trajectory of the pristine and Cu-complexed PDA (hydrogens are omitted for clarity).

In general, the number of Cu–O bonds rapidly increases overtime. After 10 ps, the number of O atoms coordinating all Cu atoms in the system is equal to 3 or 4 and such a situation is preserved across the whole trajectory later (Fig. 6a). Moreover, there is also a viable complexation via N atoms in the amine group. On average, 3 of the 4 Cu atoms in the box exhibit single coordination with N and for some period, there is double coordination with N (Fig. 6b). This behaviour is also captured on the coordination number histograms, where across the whole trajectory, the Cu atom has 4 O neighbours and a single N neighbour (Fig. 6c, d). Compared to the folding dynamics of the monomer ensemble without added Cu atoms, the number of O neighbours (all atom types) increases from 4 to 5 on average. In other words, the introduction of the Cu atoms to the simulation box leads to one additional neighbour for every O atom in the cell (Fig. 6e). The last result reflecting the complexation is an increased value of the O–O bonds' radial distribution (Fig. 6f). There is a markedly higher magnitude of O–O bonds with a 2 Å length (primary complexation) and with a 3–4 Å length, suggesting crosstalk between complexation centres. Overall, there is evidence of a pseudo-octahedral environment of the Cu atom with fivefold coordination, which is in agreement with the majority of the literature data on Cu(II) complexes with various ligands [81, 82]. The last frames of the trajectory for the pristine and Cu-loaded PDA can be seen in Fig. 6g, h, respectively. The initial frame used for the NVT propagation is contained in the SI (Fig. S7).

A secondary observation from the same complexation trajectory is the higher compactness of the Cu-loaded PDA (Fig. S8). Although there are no major changes in the C–C distribution function after introduction of the Cu (which is in line with XPS observations in the C 1s region), there is a slight but significant shift of the dominant C–N bond length from 2.6 Å to 2.4 Å. This outcome suggests a greater probability of contact between the amine group and other carbon when the PDA is enriched by copper. Moreover, there is an elevated magnitude of the C–N interactions with the higher distance and additional small maxima for 2.8 Å and 3.0 Å, indicating non-covalent bonds between PDA units is enhanced as well. Presumably, as a result of Cu complexation, a facilitated geometry for the Michael cyclisation and crosslinking is created via closer C–N contact. As a result of those two factors (stronger non-covalent interactions and higher propensity for crosslinking)

the Cu-loaded PDA is expected to be thicker than the pristine PDA, which was reported on the SEM images and XPS spectra beforehand. Additional arguments for higher compactness are the slightly higher number of C–C neighbours (with a 4-Å cutoff) emerging after 10 ps of the simulation (Fig. S8b), increased mass density and reduced void size distribution in the cell (Figs. S8b–d, respectively).

ReaxFF simulations were performed for various parametrisations available in the literature for benchmarking purposes (Figs. S9–S13). The parametrisation taken initially for the ReaxFF model was ReaxFF\_CHONSMgPNaCuCl\_2013\_2 [83]. It was chosen because the results of the complexation simulations gave the results of the highest agreement with the chemical intuition. In particular, most of the available parametrisation result in a seemingly strange description of the Cu–Cu interactions leading to creation of the Cu–Cu dimers. In fact, the coordination environment of the Cu atoms has a notable dependence on the chosen parametrisation (see discussion in the SI file).

Per analogy, simulations with varying sizes of the box with fixed number of atoms have been performed to investigate the effect of the periodic boundary conditions on the result (Figs. S14–S15). The box used in the first version of the paper had dimensions: 3.0 nm × 3.0 nm × 3.0 nm with the density of 0.15 g/cm<sup>3</sup> and 323 atoms in total. This was designed as sparse box, so that the periodic images of the molecules do not see each other and the process of Cu complexation is captured in isolation. Effectively, this setup corresponds to the conditions where the metal-coordinated polymer floats in the vacuum. We have performed analogous simulation in smaller boxes to verify the influence of the periodic images on the complexation process. In the first case with dimensions 2.5 nm × 2.3 nm × 2.2 nm (density 0.35 g/cm<sup>3</sup>), copper atoms results in a small cluster surrounded by the dopamine molecules. In the latter case with 2.5 nm × 2.0 nm × 1.8 nm (density 0.5 g/cm<sup>3</sup>), the cluster did not emerge. Per analogy to the sparse box, there is one amine group per copper atom on average and other ligands are oxygens. However, due to the steric hindrance (induced by the presence of periodic images), coordination number of the Cu exceeded 5 and could range even to 8 for some frames in the trajectory (3 Å cutoff for the Cu–O and Cu–N bonds). The overall geometry and the  $\pi$ – $\pi$  interactions within the dopamine units are preserved, though.

Finally, simulations for a  $4 \times$  larger and  $16 \times$  larger system have been also performed (Figs. S16-S17). In the enlarged system with ca. 2600 atoms and box size  $6 \text{ nm} \times 6 \text{ nm} \times 6 \text{ nm}$  the coordination profile is similar compared to the simulation in the smaller system (Fig. S16). Most of the copper atoms are surrounded by  $4 \pm 1$  oxygens from quinones and  $1 \pm 1$  nitrogen from amine groups (on average, throughout the trajectory). Of course, as the system is larger, higher and lower coordination numbers become also possible. The structure after 100 ps is also compact, and Cu atoms are embedded inside. Actually, this size of the system is on the similar order as in the experiment (typically several nm thickness of the coating).

However, when the system is further enlarged to  $12 \text{ nm} \times 12 \text{ nm} \times 12 \text{ nm}$  box, there is a major divergence of the result compared to other (Fig. S17). Namely, the structure is partially destroyed during the 300 K NVT trajectory with molecules such as acetylene, CO and  $\text{CH}_4$  being produced. Additionally, some of the Cu atoms with unsaturated valency are formed outside

the main polymer ball. Regardless of the destruction, the coordination structure of the Cu atoms in the whole system (on average) seems to be similar to the previous cases."

### Optical properties of the transition metal-loaded PDA

The Raman spectra of  $\text{TiO}_2$  nanotubes presented in Fig. 7a–c (black plots) are typical for anatase phase signals corresponding to  $E_{g(1)}$  ( $143 \text{ cm}^{-1}$ ),  $E_{g(2)}$  ( $197 \text{ cm}^{-1}$ ),  $B_{1g}$  ( $394 \text{ cm}^{-1}$ ),  $A_{1g}$  ( $514 \text{ cm}^{-1}$ ) and  $E_{g(3)}$  ( $634 \text{ cm}^{-1}$ ) [84]. Those peaks are also observed for modified samples with lower intensity, indicating that the polymer film covers the titania substrate, weakening the signals. After the deposition of PDA onto the HNTs, two additional strong bands at  $1350 \text{ cm}^{-1}$  and  $1580 \text{ cm}^{-1}$  appear. Their presence is attributed to the vibration of aromatic rings and aliphatic C–C and C–O stretching [85] or to pyrrole-ring stretching and C=C backbone stretching [86]. Notably, there is also a baseline

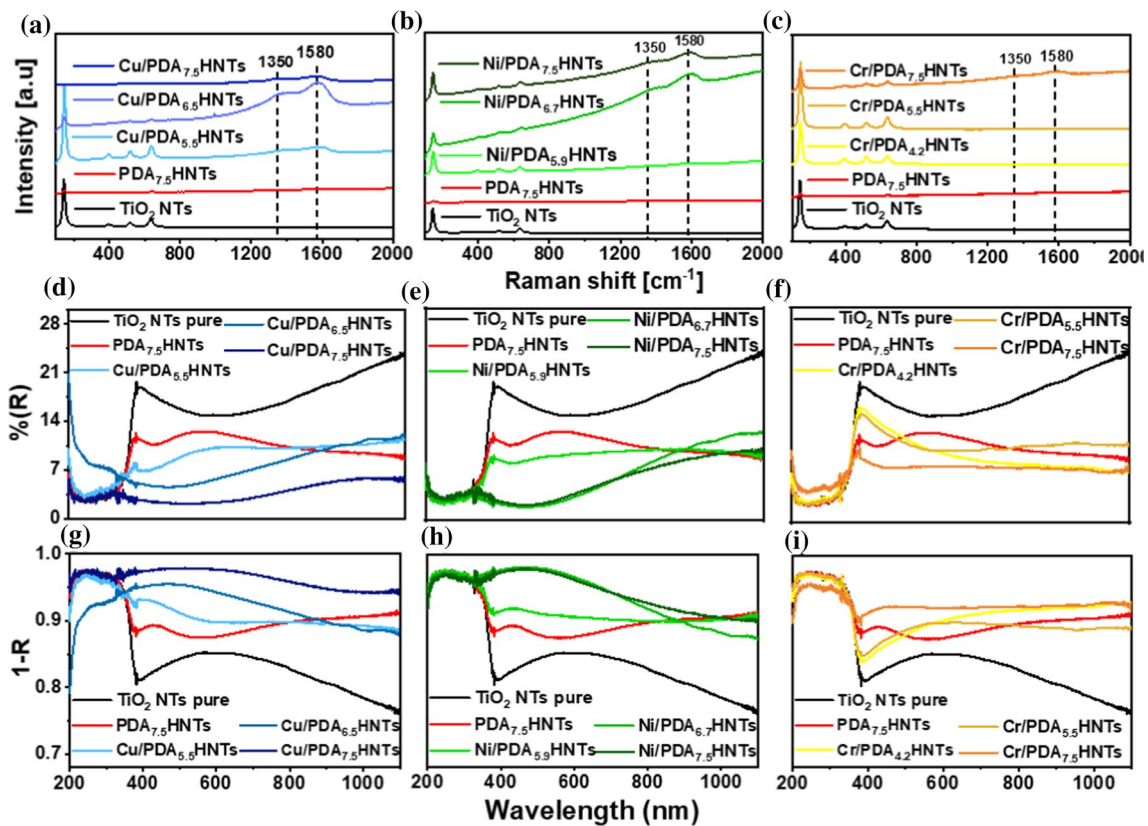


**Figure 7** Raman spectra of nanotubes with polydopamine electrodepositing in the presence of (a)  $\text{Cu}^{2+}$ , (b)  $\text{Ni}^{2+}$ , (c)  $\text{Cr}^{3+}$  ions in the electrolyte, UV-Vis spectra of nanotubes with poly-

dopamine electrodepositing in the presence of (d)  $\text{Cu}^{2+}$ , (e)  $\text{Ni}^{2+}$ , (f)  $\text{Cr}^{3+}$  ions, 1-R plots of nanotubes with polydopamine electrodepositing in the presence of (g)  $\text{Cu}^{2+}$ , (h)  $\text{Ni}^{2+}$ , (i)  $\text{Cr}^{3+}$  ions.

increasing trend associated with fluorescence of the PDA [87], which varies depending on the synthesis pH and the metal type. Differences in the  $1350\text{ cm}^{-1}$  and  $1580\text{ cm}^{-1}$  bands intensity and the magnitude of fluorescence result from the variable thickness of the deposited PDA film [55]. This effect is particularly visible for samples containing chromium species (Fig. 7c yellow lines). In case of the materials containing Cu (Fig. 7a blue lines) and Ni (Fig. 7b green lines), the intensity of the described peaks at  $1350\text{ cm}^{-1}$  and  $1580\text{ cm}^{-1}$  is much higher than the value recorded for the reference PDA sample. The intensity of the fluorescence recorded in the Raman spectra is not proportional to the increase in the pH solution used for electropolymerisation. This indicates that the fluorescence intensity depends less on the thickness of the layer itself and more on the structural differences of the PDA layers in the composite materials and effectively on the fabrication conditions. In particular, the content of the indole-5,6-quinone, as a PDA structural unit, results in a highly fluorescent structure [88]. XPS analysis (see X-ray photoelectron spectroscopy results) confirmed the presence of this structure as dominant for the samples with higher fluorescence.

Reproducibility of Raman spectra has been verified by measuring of 6 samples for each metal-modified electrodes (Fig. S18). In the case of Cr-based modifications, there are no differences, and signal from the PDA is smallest. This results from the small thickness of the PDA for those modifications. In the case of Cu-based and Ni-based modifications, the shape is qualitatively the same for all samples. The difference between samples is basically the slope of the fluorescence baseline, which is a function of both the material properties (PDA thickness in particular) but also the surface topography. Nevertheless, one can conclude that samples are synthesised repeatable in terms of Raman signal and associated vibrational structure of the deposited molecules.

The reflectance spectra of bare titania nanotubes (Fig. 7d–f black plot) exhibit absorption edge in the UV around 300–350 nm and the characteristic reflectance dip in the visible range near 600 nm [28]. The low reflectance in the UV range results from the activity of the titania support, which absorbs mainly UV radiation [89]. After deposition of PDA film (Fig. 7d–f red plot), one can find a reflectance dip located at ca. 450 nm, which is most presumably caused by the light absorbance of the polymer, related to the structure of conjugated  $\pi$ - $\pi$  bonds. For samples

electropolymerised in the presence of metal ions, the intensity of the dips in the visible range increases and the change is more prominent when the synthesis process was carried out in a more alkaline pH. This is a consequence of the presence of a thicker PDA layer, confirming the catalytic effect of the Cu and Ni metal ions [21] on the efficient polymerisation. In addition, the presence of different metal ions changes the position of the bands typical for PDA towards higher wavelengths, which is also reported by other authors [90]. This also suggests alteration of the PDA electronic structure by the metal ions that are abundant inside the coating towards lower HOMO–LUMO gaps. It is, therefore, anticipated that such visible enhancement could improve the  $\text{TiO}_2$  photocurrent generation in the visible range.

The presence of copper-loaded (Fig. 7d) results in a much higher absorbance compared to the bare PDA. Moreover, the spectrum of a sample obtained under the same pH conditions but with the addition of nickel ions (Fig. 7e) has a slightly less intense and narrower peak found in the 420–470 nm range. The lower reflectance of the prepared metal/PDA junctions (Fig. 7 d blue plots; Fig. 7e green plots) compared to PDA electropolymerised without metal ions (Fig. 7 red plot) is also the result of the formation of dopamine complexes with metals, for which the maximum absorbance is 596–605 nm for copper [91] and 590 nm for the complex with nickel [92]. The slightly lower reflectance for the Ni/PDA samples in this range could be related to the lower capability of complex formation compared to the Cu/PDA complexes [92]. The spectra recorded for Cr-loaded samples (Fig. 7 c yellow) are characterised by higher reflectance, which suggests inefficient deposition of the organic film over the titania nanostructure described in the previous section, especially for samples prepared at lower pH values. Alternatively, the deposited film exhibits unfavourable energy level alignment with the  $\text{TiO}_2$ , such that absorption is hindered. The most evident case of this can be found for the samples fabricated at pH 4.2 and 5.5, as the characteristic dopamine peak is not visible. Kubelka–Munk plots created from reflectance data are given in Fig. S19 for comparison.

A series of DFT calculations were performed attempting to explain the difference between the behaviour of chromium with respect to other two metals. A set of complexes was built with Cr(III), Cu(I), Cu(II), Ni(II) and Ni(III) metal atoms (according to the XPS analysis) and oxidised (IQ) or reduced (DHI) PDA



units. Initial geometries were based on the literature data on similar compounds in different solvents and were DFT-optimised using dispersion. Images of the models are contained in the SI file (Figs. S20–S24). DOS spectra of corresponding complexes are given in SI file (Figs. S25–S28) in spin-polarised and unpolarised versions with a through discussion. The effect of D3 dispersion correction is discussed in the SI file (Fig. S29 and Table S5 in particular).

The overall conclusion from the calculations is that Cr complexes exhibit markedly different effect on the electronic structure than the other two, regardless whether the system is spin-polarised or not. Cu(I), Cu(II), Ni(II) and Ni(III) complexes tend to slightly narrow the band gap and increase the density of states near the valence band (HOMO level). This might lead to increased optical absorption. DOS of the Cr(III) complex however, exhibits the Fermi level inside a series of bands, where the HOMO–LUMO gap is basically absent. Thus, it is difficult to predict the Cr(III) influence on the optical absorption in general. It should be noted that conclusions taken from such DFT

calculations are far from reflecting the true behaviour of the studied system. While in the real experiment, the polymer is deposited on the (nanostructured) titania surface and a cross-talk between metal centres not considered in the simplified model. The overall message is rather to show a different electronic characteristics of the Cr(III) complexes with PDA than the other two metals.

### Photoelectrochemical properties

All photoelectrochemical measurements were taken consecutively for each sample without replacing the electrolyte or adding other substances. CV curves registered in dark conditions in 0.5 M Na<sub>2</sub>SO<sub>4</sub> are shown in Fig. 8 (left column). In the applied potential window, current is mostly capacitive, the increase of which is related to the coating of the electrode with polydopamine [17]. In addition, the presence of embedded metals can introduce additional energy levels to the semiconductor structure, which can reduce or increase its electrical resistance and affect its ability

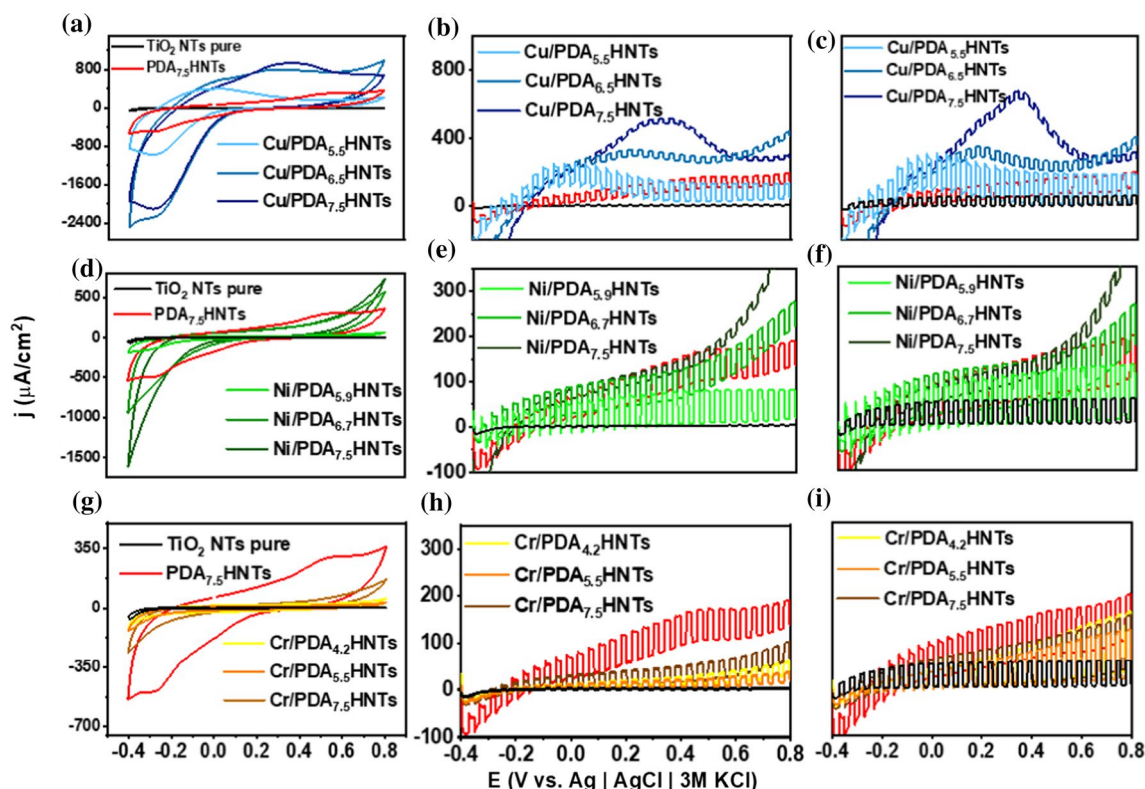


**Figure 8** Cyclic voltammetry measurement taken without irradiation in 0.5 M Na<sub>2</sub>SO<sub>4</sub> solution (left column), linear voltammetry measurement with visible light irradiation and linear voltam-

metry measurement (middle column), with UV–Vis irradiation (right column) performed for Cu (a, b, c); Ni (d, e, f); Cr (g, h, i) samples.

to carry Faradaic current [87]. The photoelectrochemical response was investigated by performing linear sweep voltammetry measurements in different light conditions: visible (middle column) or UV–Vis radiation (right column).

For the bare titania nanotubes, the registered CVs (black plot) show a very low capacitive current across the whole investigated potential range and a very low photocurrent response. Removing the UV cut-off optical filter increased the current (black plots), but the photoactivity was still not prominent due to the wide band gap, limiting light absorption mostly to the ultraviolet range [27].

The heterojunction obtained after dopamine electropolymerisation on the hydrogenated  $\text{TiO}_2$  surface exhibited a greater capacitive current, especially in the anodic region (Fig. 8, red plot). More importantly however, the inorganic/organic electrode materials generated a higher photocurrent both under vis (Fig. 8 b red plot) and UV–Vis (Fig. 8 c red plot) light, which is related to the high capacitance and strong light absorption typical for this material as a  $\pi$ -conjugated organic junction [27]. In the obtained junction, the use of polymer networks blocks the dissolution of the electrolyte, which is supposed to limit the recombination of charges, [93]. On voltammograms recorded for the PDA<sub>7.5</sub>HNTs sample, peaks characteristic of dopamine oxidation and reduction are still visible, as was noted during the electropolymerisation process. Their presence could be assigned to catechol-quinone redox pairs constituting the PDA structure [1].

Such a photocurrent-boosting property of the PDA can be useful in many applications such as photoelectrochemical water splitting and photo-driven sensing of organic molecules [94]. PDA can serve as a binder for dopants, as well as a photocurrent enhancer itself as an alternative to, e.g. surface plasmon-resonance approaches.

For the samples measured in the presence of Cu(II) ions, the CV curves (Fig. 8 a) showed higher oxidation and reduction currents compared to  $\text{TiO}_2$  NTs and the sample with pure PDA. The recorded current increased with the pH of the solution during electropolymerisation. On the voltammograms, an oxidation peak at the potential of 0.0 V shifted towards higher potential values as the electrolyte pH increased. The reduction peak registered at  $-0.3$  V did not change its position regardless of the pH of the electrolyte used for the polymerisation process. Measurements taken by linear voltammetry when the working electrode

was exposed to the visible (Fig. 8b) and UV–Vis (Fig. 8c) irradiation showed the highest photocurrent values for the sample prepared at the lowest pH = 5.5. The increase in photocurrent, especially in visible light irradiation, was related to the light increasing absorption also from visible range, as confirmed by the UV–Vis spectra (Fig. 7). As the pH value increased, the photocurrent notably fell, presumably due to the higher coating thickness and thus reduced illumination of the junction area. However, an increasingly higher non-photocurrent was noted compared to the bare titania. This feature is consistent with the shape of dark CVs and was a result of the developed surface area with Cu(I)/Cu(II)-containing sites, where charge could be accumulated and Faradaic process occur. Peak potentials for those processes were located at 0.0 V for CuPDA<sub>5.5</sub>HTNs, +0.2 V for CuPDA<sub>6.5</sub>HTNs and +0.3 V for CuPDA<sub>7.5</sub>HTNs and shifted towards higher potentials with increasing pH of the synthesis.

In the case of the sample prepared in the presence of nickel ions at pH 5.9, recorded dark currents on the CVs (both oxidation and reduction) were lower than those observed for pure PDA (Fig. 8 d). Again, in a more alkaline pH, the value of both the oxidation current +0.8 V and the reduction current  $-0.4$  V increased significantly, indicating a higher surface area developed during the synthesis due to the facilitated Michael reaction and higher PDA yield. The recorded photocurrents for visible (Fig. 8e) and UV–Vis (Fig. 8f) light irradiation were the highest for the sample when the organic layer was deposited at the lowest pH—similarly as in the Cu case. Analogously, a trend of decaying photocurrent with increasing pH was also noted for the samples obtained in the presence of nickel ions. The nickel/PDA junction was also characterised by an increase in capacitive current for potential values from 0.0 V, similar to the voltammogram recorded for pure PDA. However, it grew even more at +0.5 V, which is related to the oxidation reaction of  $\text{Ni}^{2+}$  to  $\text{Ni}^{3+}$  [95]. The increase of the current density in this region might also correspond to the onset of the oxygen evolution reaction that is characteristic of nickel-based catalysts [35]. It is worth underlining the significant increase in reduction currents when polarisation was carried out towards  $-0.4$  V, especially for the sample obtained in the electrolyte with the highest pH. Such a distinctive behaviour indicates the strong propensity of the obtained material towards hydrogen evolution reaction, similar to other Nickel-based catalysts.

On the other hand, for Cr/PDAHNTs junctions, both capacitive currents, and photocurrents do not vary significantly with respect to the synthesis pH. In the CV curves, the currents are much lower (Fig. 8g) than the reference PDA-covered titania sample. The photocurrents (Fig. 8) recorded during visible light irradiation were also lower compared to the reference PDA-modified titania, although the correlation between higher photocurrent and higher synthesis pH was preserved. Overall, for the Cr-modified junctions, the photoactivity boost in visible light was the weakest.

For the junctions prepared in the presence of copper and nickel ions, there was an inversely proportional relation between the capacitive current and recorded reflectance, which depended on the thickness of the PDA layer. This indicates that capacitive currents scale monotonously with the thickness of the polymer—being contrary to the intuition based on the parallel plate capacitor—as also described by other groups [96]. However, the recorded photocurrent of the obtained sample was inversely proportional to the polymer thickness. This was presumably due to the increase in the diffusion length of the generated exciton within a thicker polymer film, which resulted in a lower probability of efficient charge collection at the bottom of the electrode [97]. The detailed values of the PDA layer thicknesses for individual samples were determined on the basis

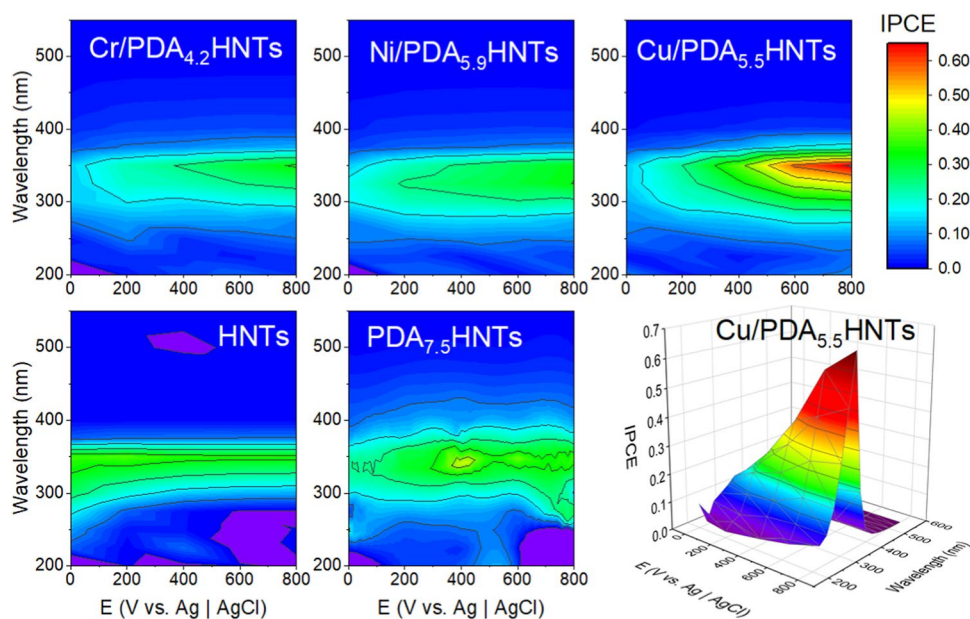
of the XPS and SEM analysis (Table 1), as already discussed.

Reproducibility of the CV curves registered in the dark conditions after electropolymerisation has been also checked (Fig. S30). The issue of surface area uncertainty—and thus current magnitude uncertainty—is analogous as in the case of electropolymerisation reproducibility test.

### IPCE action maps and reproducibility of the metal-loaded samples

The IPCE action map recorded for pure TiO<sub>2</sub> nanotubes (Fig. 9) shows a characteristic UV band with a maximum around 350 nm (peaking at 30% efficiency) over the entire polarisation range [98]. After coating the nanotubes with polydopamine, a moderate increase in quantum yield was recorded at the wavelengths in the range 350–400 nm. This outcome is in parallel with our previous results for PDA/NTs junctions with loosely spaced nanotubes [51], and in line with the higher photocurrent values recorded for this sample (Fig. 8 red plots). In the case of samples electropolymerised in the presence of Cr and Ni metals, the behaviour is rather similar. However, in the case of Cu, the IPCE value at the maximum is doubled (63% efficiency) in the region of anodic polarisation. This outcome suggests a strong positive influence of Cu ions on the electron–hole separation efficiency and enables recombination suppression, provided the

**Figure 9** Comparison of quantum efficiency action maps for metal-loaded PDA with reference PDA and pristine HNT electrodes.



bias-induced electric field is sufficient. While the IPCE relation to the wavelength remains similar in all cases, the 3D view shows significant, quasi-linear dependence on the polarisation for Cu. Samples taken for this measurement were synthesised in the lowest pH, due to highest photocurrents observed in Fig. 8.

Moreover, the reproducibility of the IPCE/photocurrent results has been performed. Three action maps have been recorded for low-pH synthesised metal-loaded PDA samples, 3 samples for each metal (9 maps in total). The result is given in Fig. S31 in the SI file. In the case of Ni-based modifications, three individual samples exhibit qualitatively the same shape of the action map, with the maximum roughly at 350 nm in the range between 25 and 33%. The influence of anodic polarisation on the photocurrent efficiency is positive in all cases. It is to be noted that there are erroneous data points in the regime of low wavelengths (ca. 250 nm) for some part of samples. Their physical origin is largely unknown, but they are understandable as the 250 nm equal to 5 eV largely exceeds the band gap of the electrodes. The same kind of error was also recorded in the case of Cr-based modification (Sample 3). In the case of Cu-based modifications, trends are fully analogous and the spread of the IPCE maxima is within the 55% and 63%. Finally, in the case of Cr-based modifications, spread is larger (20% to 32%), because those modifications result in lowest magnitudes of photocurrents. A notable spread of values is related to the randomness and stochasticity of the synthesis procedures. Therefore, a more detailed photocurrent statistics have been collected by taking 6 photocurrent measurements for each metal type at isolated wavelengths being equal to 350 nm, 400 nm and 450 nm to investigate the deviation in the photocurrents in various regions of the spectrum (Fig. S32). In general, photocurrent magnitudes are small (below 1  $\mu\text{A}$ ), because the information is gathered only from the small part of the spectrum (the width of the pulse coming out of the monochromator is roughly equal to 2 nm). Table S6 with statistical data is given in the SI file.

In most cases, the relative errors are on the order of 10%, except the Cr-350 nm, which originates from the sample preparation randomness and surface area uncertainty. Typically the mean is almost identical to the median, and they lie in the middle of the max–min interval, which indicates the symmetric character of the distribution. The box plot with interquartile ranges (i.e. distances between the third and first quartile) shows

that 350 nm and 450 nm data are have relatively narrow spread of data compared to 400 nm. The physical reason for that occurrence might be that this region is a transition zone between absorption by the titania and the polymer. Outliers significantly exceeding the 1.5 IQR are present only in the case of Cr-400 nm samples set.”

Further investigation of the properties of the metal-loaded PDA requires a thorough experimental and computational analysis with a comprehensive multi-scale computational model. A possible solution to handle a large complexity of the system (surface–polymer–metal ions–electrolyte) is to use machine-learned potentials (MLIPs). This approach has been successfully used in prediction of many properties, e.g. mechanical, thermal, electrical and bridging the gap between first-principle calculations and continuous models [99, 100].

## Conclusions

In this study, we introduced and characterised a novel approach for enhancing photoelectrochemical performance through the electropolymerisation of polydopamine (PDA) on titania nanotubes, incorporating transition metal complexes (Cu, Ni, and Cr) with properties modulated by the electrolyte’s pH. Higher pH values resulted in thicker PDA layers and higher oxidation states of metals, enhancing Michael cyclisation. Metal complexation increased structural compactness, predominantly through oxygen–metal bonds. Additionally, the metal modification notably improved visible light absorption, particularly for Cu and Ni complexes, as confirmed by experiments and supported by density functional theory calculations. However, overly thick PDA layers hindered photocurrent generation. Optimisation in acidic conditions caused markedly boosted photocurrent quantum efficiency to 20% at 400 nm of the Cu-modified nanotubes. Furthermore, the presence of d-metal salts during electropolymerisation catalytically influenced PDA formation, underscoring the significant impact of salt type on both the deposition and photoelectrochemical properties of PDA.

## Acknowledgements

This work has received financial support from the Polish National Science Centre: Grant No. 2017/26/E/ST5/00416 and the Polish Ministry of Science and Education under grant number DI2019 017649.

## Author contributions

KP was involved in the conceptualisation, methodology, formal analysis, investigation, data curation, writing—draft, and visualisation; AO contributed to the conceptualisation, methodology, validation, resources, writing—draft, visualisation, project administration, and funding acquisition; JG assisted in the formal analysis and investigation; AK contributed to the formal analysis and investigation; JK performed the formal analysis and investigation; KS contributed to the validation, resources, writing—review and editing, supervision, project administration, and funding acquisition.

## Data availability

Data are available from authors on request.

**Supplementary Information** The online version contains supplementary material available at <https://doi.org/10.1007/s10853-024-09722-1>.

**Open Access** This article is licensed under a Creative Commons Attribution 4.0 International License, which permits use, sharing, adaptation, distribution and reproduction in any medium or format, as long as you give appropriate credit to the original author(s) and the source, provide a link to the Creative Commons licence, and indicate if changes were made. The images or other third party material in this article are included in the article's Creative Commons licence, unless indicated otherwise in a credit line to the material. If material is not included in the article's Creative Commons licence and your intended use is not permitted by statutory regulation or exceeds the permitted use, you will need to obtain permission directly from the copyright holder. To view a copy of this licence, visit <http://creativecommons.org/licenses/by/4.0/>.

## References

- [1] Olejnik A, Ficek M, Siuzdak K, Bogdanowicz R (2022) Multipathway mechanism of polydopamine film formation at vertically aligned diamondised boron-doped carbon nanowalls. *Electrochim Acta* 409:140000. <https://doi.org/10.1016/j.electrochim.2022.140000>
- [2] Khan Z, Shanker R, Um D et al (2018) Bioinspired polydopamine and composites for biomedical applications. *Electr Conduct Polym Polym Compos* 1:1–29. <https://doi.org/10.1002/9783527807918.ch1>
- [3] Wang Z, Yang H, He F et al (2019) Mussel-inspired surface engineering for water-remediation materials. *Matter* 1:115–155. <https://doi.org/10.1016/j.matt.2019.05.002>
- [4] Garc JC, Rosu H, Jasso- AB (2023) Kinetic study of polydopamine sphere synthesis using TRIS: relationship between synthesis conditions and final properties. *RSC Adv* 9:5081–5095. <https://doi.org/10.1039/D2RA06669F>
- [5] Scheidt HA, Filip C, Turcu R et al (2013) Structure of polydopamine: a never-ending story? *Langmuir* 29:10539–10548. <https://doi.org/10.1021/la4020288>
- [6] Zhang X, Huang Q, Deng F et al (2017) Mussel-inspired fabrication of functional materials and their environmental applications: Progress and prospects. *Appl Mater Today* 7:222–238. <https://doi.org/10.1016/j.apmt.2017.04.001>
- [7] Loget G, Eun J, Mazare A et al (2015) Highly controlled coating of a biomimetic polymer in TiO<sub>2</sub> nanotubes. *Electrochem Commun* 52:41–44. <https://doi.org/10.1016/j.elecom.2015.01.011>
- [8] Fredi G, Simon F, Sychev D et al (2020) Bioinspired polydopamine coating as an adhesion enhancer between para FFI n microcapsules and an epoxy matrix. *ACS Omega* 5:19639–19653. <https://doi.org/10.1021/acsomega.0c02271>
- [9] Zheng D, Huang C, Zhu X (2021) Performance of polydopamine complex and mechanisms in wound healing. *Int J Mol Sci* 22:10563. <https://doi.org/10.3390/ijms221910563>
- [10] Meredith P, Sarna T (2006) The physical and chemical properties of eumelanin. *Pigment Cell Melanoma Res* 19:549–659. <https://doi.org/10.1111/j.1600-0749.2006.00345.x>
- [11] Eom T, Lee J, Lee S et al (2022) Highly conductive polydopamine coatings by direct electrochemical synthesis on Au. *ACS Appl Polym Mater* 4:5319–5329. <https://doi.org/10.1021/acsapm.2c00317>
- [12] Cui Z, Marcelle S, seukep alix, Zhao M, et al (2022) Thermoplastic polyurethane/titania/polydopamine(TPU/TiO<sub>2</sub>/PDA) 3-D porous composite foam with outstanding oil/water separation performance and photocatalytic dye degradation. *Adv Compos Hybrid Mater* 5:2801–2816. <https://doi.org/10.1007/s42114-022-00503-5>
- [13] Wang Y, Yang D, Hessien MM et al (2022) Flexible barium titanate@polydopamine/polyvinylidene fluoride/polymethyl methacrylate nanocomposite films with high performance energy storage. *Adv Compos Hybrid Mater* 5:2106–2115. <https://doi.org/10.1007/s42114-022-00552-w>
- [14] Cui Z, Zhou J, Wang X et al (2023) In situ growth of bimetallic nickel cobalt sulfide (NiCo<sub>2</sub>S<sub>4</sub>) nanowire arrays encapsulated by nitrogen-doped carbon on carbon cloth as binder-free and flexible electrode for high-performance aqueous Zn batteries. *Adv Compos Hybrid Mater* 6:95. <https://doi.org/10.1007/s42114-023-00668-7>
- [15] Li H, Xi J, Donaghue AG et al (2020) Synthesis and catalytic performance of polydopamine supported metal nanoparticles. *Sci Rep* 10:1–7. <https://doi.org/10.1038/s41598-020-67458-9>
- [16] Zhang X, Huang Q, Liu M et al (2015) Applied Surface Science Preparation of amine functionalized carbon nanotubes via a bioinspired strategy and their application in Cu<sup>2+</sup> removal. *Appl Surf Sci* 343:19–27. <https://doi.org/10.1016/j.apsusc.2015.03.081>

- [17] Wang N, Zhang Z, Huang J, Hu Y (2019) Facile synthesis of copper ions chelated sand via dopamine chemistry for recyclable and sustainable catalysis. *Chem Eng Sci* 203:312–320. <https://doi.org/10.1016/j.ces.2019.04.009>
- [18] Xu Q, Chang M, Zhang Y, Wang E (2020) PDA / Cu bioactive hydrogel with “hot ions effect” for inhibition of drug-resistant bacteria and enhancement of infectious skin wound healing. *ACS Appl Mater Interfaces* 12:31255–31269. <https://doi.org/10.1021/acsami.0c08890>
- [19] Bhattacharjee S, Ali A, Ahn WS (2021) Heterogeneous Aza—Michael Addition Reaction by the Copper—Based Metal—Organic Framework (CuBTC). *Catal Letters* 151:2011–2018. <https://doi.org/10.1007/s10562-020-03459-7>
- [20] Xu L-W, Li L, Xia C-G (2004) Transition-metal-based lewis acid catalysis of Aza-type Michael additions of amines to  $\alpha$ ,  $\beta$ -unsaturated electrophiles in water. *Helv Chim Acta* 87:1552–1526. <https://doi.org/10.1002/hlca.200490139>
- [21] Comelles J, Moreno-mañas M, Vallribera A (2005) Michael additions catalyzed by transition metals and lanthanide species. *A Rev Arkivoc* 2005:207–238. <https://doi.org/10.3998/ark.5550190.0006.921>
- [22] Liu C, Bai Y, Li W et al (2022) In situ growth of three-dimensional mxene/metal-organic framework composites for high-performance supercapacitors. *Angew Chemie Int Ed*. <https://doi.org/10.1002/anie.202116282>
- [23] Li W, Guo X, Geng P et al (2021) Rational design and general synthesis of multimetallic metal-organic framework nanooctahedra for enhanced Li-S battery. *Adv Mater* 33:2105163. <https://doi.org/10.1002/adma.202105163>
- [24] Zhou H, Zhu G, Dong S et al (2023) Ethanol-Induced Ni<sup>2+</sup>-intercalated cobalt organic frameworks on vanadium pentoxide for synergistically enhancing the performance of 3D-printed micro-supercapacitors. *Adv Mater* 35:2211523. <https://doi.org/10.1002/adma.202211523>
- [25] Zhang C, Ou Y, Lei W-X et al (2016) CuSO<sub>4</sub>/H<sub>2</sub>O<sub>2</sub>-induced rapid deposition of polydopamine coatings with high uniformity and enhanced stability. *Angew Chemie Int Ed* 55:3054–3057. <https://doi.org/10.1002/anie.201510724>
- [26] Yang L, Kong J, Zhou D et al (2014) Transition-metal-ion-mediated polymerization of dopamine: mussel-inspired approach for the facile synthesis of robust transition-metal nanoparticle-graphene hybrids. *Chem A Eur J* 20:7776–7783. <https://doi.org/10.1002/chem.201402241>
- [27] Haryński Ł, Grochowska K, Karczewski J et al (2020) Scalable route toward superior photoresponse of UV-laser-treated TiO<sub>2</sub> nanotubes. *ACS Appl Mater Interfaces* 12:3225–3235. <https://doi.org/10.1021/acsami.9b19206>
- [28] Wawrzyniak J, Grochowska K, Karczewski J et al (2020) The geometry of free-standing titania nanotubes as a critical factor controlling their optical and photoelectrochemical performance. *Surf Coat Technol* 389:125628. <https://doi.org/10.1016/j.surfcoat.2020.125628>
- [29] Algadi H, Ren J, Alqarni A (2023) Solution-processed nitrogen-doped graphene quantum dots/perovskite composite heterojunction for boosting performance of anatase titanium dioxide (TiO<sub>2</sub>)-based UV photodetector. *Adv Compos Hybrid Mater* 6:86. <https://doi.org/10.1007/s42114-023-00667-8>
- [30] Chen T, Wang Y, Zhang P et al (2023) Targeted synthesis of hollow titania microspheres with sustained release behaviors of 1,2-benzisothiazolin-3-one (BIT) for good marine antifouling performance. *Adv Compos Hybrid Mater* 6:151. <https://doi.org/10.1007/s42114-023-00722-4>
- [31] Sirimekanont T, Supaphol P, Sombatmankhong K (2023) Titanium (IV) oxide composite hollow nanofibres with silver oxide outgrowth by combined sol-gel and electrospinning techniques and their potential applications in energy and environment. *Adv Compos Hybrid Mater* 6:115. <https://doi.org/10.1007/s42114-023-00690-9>
- [32] Zhou Z, Liang Y, Xing X-S et al (2023) Integration of cobalt-phosphate catalyst and titanium dioxide interlayer in the hematite photoanodes to improve photoelectrochemical water splitting for hydrogen production. *Adv Compos Hybrid Mater* 6:94. <https://doi.org/10.1007/s42114-023-00677-6>
- [33] Li J, Wang Y, Song H et al (2023) Photocatalytic hydrogen under visible light by nitrogen-doped rutile titania graphitic carbon nitride composites: an experimental and theoretical study. *Adv Compos Hybrid Mater* 6:83. <https://doi.org/10.1007/s42114-023-00659-8>
- [34] Nischk M, Mazierski P, Wei Z, Siuzdak K (2016) Enhanced photocatalytic, electrochemical and photoelectrochemical properties of TiO<sub>2</sub> nanotubes arrays modified with Cu, AgCu and Bi nanoparticles obtained via radiolytic reduction. *Appl Surf Sci* 387:89–102. <https://doi.org/10.1016/j.apsusc.2016.06.066>
- [35] Momeni MM, Ghayeb Y (2015) Photoelectrochemical water splitting on chromium-doped titanium dioxide nanotube photoanodes prepared by single-step anodizing. *J Alloys Compd* 637:393–400. <https://doi.org/10.1016/j.jallcom.2015.02.137>
- [36] Devi LG, Kavitha R (2016) A review on plasmonic metal – TiO<sub>2</sub> composite for generation, trapping, storing and dynamic vectorial transfer of photogenerated electrons across the Schottky junction in a photocatalytic system. *Appl Surf Sci* 360:601–622. <https://doi.org/10.1016/j.apsusc.2015.11.016>
- [37] Parnicka P, Lisowski W, Klimczuk T, et al (2019) A new simple approach to prepare rare-earth metals-modified TiO<sub>2</sub> nanotube arrays photoactive under visible light: Surface properties and mechanism investigation. *Results Phys* 12:412–423. <https://doi.org/10.1016/j.rinp.2018.11.073>
- [38] Haryński Ł, Karczewski J, Ryl J et al (2021) Rapid development of the photoresponse and oxygen evolution of TiO<sub>2</sub> nanotubes sputtered with Cr thin films realized via laser annealing. *J Alloys Compd* 877:160316. <https://doi.org/10.1016/j.jallcom.2021.160316>
- [39] Molenda Z, Grochowska K, Karczewski J, et al (2019) The influence of the Cu<sub>2</sub>O deposition method on the structure, morphology and photoresponse of the ordered TiO<sub>2</sub>NTs/Cu<sub>2</sub>O heterojunction The influence of the Cu<sub>2</sub>O deposition method on the structure, morphology and photoresponse of the ordered T. *Mater Res Express* 6:1250b6. <https://doi.org/10.1088/2053-1591/ab6195>
- [40] Dong Z, Ding D, Li T, Ning C (2018) Ni-doped TiO<sub>2</sub> nanotubes photoanode for enhanced photoelectrochemical water splitting. *Appl Surf Sci* 443:321–328. <https://doi.org/10.1016/j.apsusc.2018.03.031>
- [41] Wang Y, Chen D, Zhang J et al (2022) Charge relays via dual carbon-actions on nanostructured BiVO<sub>4</sub> for high performance photoelectrochemical water splitting. *Adv Funct Mater* 32:2112738. <https://doi.org/10.1002/adfm.202112738>
- [42] Yang W, Prabhakar RR, Tan J et al (2019) Strategies for enhancing the photocurrent, photovoltage, and stability of photoelectrodes for photoelectrochemical water splitting. *Chem Soc Rev* 48:4979–5015. <https://doi.org/10.1039/c8cs00997j>
- [43] Jaxin L, Hao Y, Wenjie Z et al (2022) Advances in Z-scheme semiconductor photocatalysts for the photoelectrochemical applications: A review. *Carbon energy* 4:294–331. <https://doi.org/10.1002/cey2.179>
- [44] Wu J, Tao Y, Zhang C et al (2023) Activation of chloride by oxygen vacancies-enriched TiO<sub>2</sub> photoanode for efficient

- photoelectrochemical treatment of persistent organic pollutants and simultaneous H<sub>2</sub> generation. *J Hazard Mater* 443:130363. <https://doi.org/10.1016/J.JHAZMAT.2022.130363>
- [45] Okada Y (2021) Synthetic semiconductor photoelectrochemistry. *Chem Rec* 21:2223–2238. <https://doi.org/10.1002/tcr.202100029>
- [46] Chatterjee P, Ambati MSK, Chakraborty AK et al (2022) Photovoltaic/photo-electrocatalysis integration for green hydrogen: A review. *Energy Convers Manag* 261:115648. <https://doi.org/10.1016/J.ENCONMAN.2022.115648>
- [47] Santhosh Kumar R, Govindan K, Ramakrishnan S et al (2021) Fe<sub>3</sub>O<sub>4</sub> nanorods decorated on polypyrrole/reduced graphene oxide for electrochemical detection of dopamine and photocatalytic degradation of acetaminophen. *Appl Surf Sci* 556:149765. <https://doi.org/10.1016/j.apsusc.2021.149765>
- [48] Chen Z, Guan M, Cheng Y et al (2023) Boehmite-enhanced poly(vinylidene fluoride-co-hexafluoropropylene)/polyacrylonitrile (PVDF-HFP/PAN) coaxial electrospun nanofiber hybrid membrane: a superior separator for lithium-ion batteries. *Adv Compos Hybrid Mater* 6:219. <https://doi.org/10.1007/s42114-023-00794-2>
- [49] Yi P, Song Y, Liu Z et al (2023) Boosting alkaline urea oxidation with a nickel sulfide/cobalt oxide heterojunction catalyst via interface engineering. *Adv Compos Hybrid Mater* 6:228. <https://doi.org/10.1007/s42114-023-00810-5>
- [50] Sarkar D, Das N, Saikh MM et al (2023) Elevating the performance of nanoporous bismuth selenide incorporated arch-shaped triboelectric nanogenerator by implementing piezo-tribo coupling effect: harvesting biomechanical energy and low scale energy sensing applications. *Adv Compos Hybrid Mater* 6:232. <https://doi.org/10.1007/s42114-023-00807-0>
- [51] Olejnik A, Olbryś K, Karczewski J et al (2023) Band gap engineering toward semimetallic character of quinone-rich polydopamine. *J Phys Chem C* 127:12662–12677. <https://doi.org/10.1021/acs.jpcc.2c08804>
- [52] Siuzdak K, Szkoda M, Lisowska-Oleksiak A et al (2016) Highly stable organic-inorganic junction composed of hydrogenated titania nanotubes infiltrated by a conducting polymer. *RSC Adv* 6:33101–33110. <https://doi.org/10.1039/c6ra01986b>
- [53] Landi S, Segundo IR, Freitas E et al (2022) Use and misuse of the Kubelka-Munk function to obtain the band gap energy from diffuse reflectance measurements. *Solid State Commun* 341:114573. <https://doi.org/10.1016/J.SSC.2021.114573>
- [54] Atomistix Toolkit Version 2019.03, Synopsys QuantumWise A/S ([www.quantumwise.com](http://www.quantumwise.com))
- [55] Zhong S, Luo R, Wang X et al (2014) Effects of polydopamine functionalized titanium dioxide nanotubes on endothelial cell and smooth muscle cell. *Colloids Surf B Biointerfaces* 116:553–560. <https://doi.org/10.1016/J.COLSURFB.2014.01.030>
- [56] Bogdanowicz R, Ryl J, Darowicki K, Kosmowski BB (2009) Ellipsometric study of oxide formation on Cu electrode in 0.1 M NaOH. *J Solid State Electrochem* 13:1639–1644. <https://doi.org/10.1007/s10008-008-0650-z>
- [57] Serrano-Claumarchirant JF, Muñoz-Espí R, Cantarero A et al (2023) Electrochemical deposition of conductive polymers on fabrics. *Coatings* 13:383. <https://doi.org/10.3390/coatings13020383>
- [58] Kim MJ, Cruz MA, Ye S et al (2019) One-step electrodeposition of copper on conductive 3D printed objects. *Addit Manuf* 27:318–326. <https://doi.org/10.1016/j.addma.2019.03.016>
- [59] Polozhentseva J, Novozhilova M, Karushev M (2022) Reversible redox processes in polymer of unmetalated salen-type ligand: Combined electrochemical in situ studies and direct comparison with corresponding nickel metallopolymer. *Int J Mol Sci* 23:1795. <https://doi.org/10.3390/ijms23031795>
- [60] Yang AI L et al (2014) Transition-metal-ion-mediated polymerization of dopamine mussel-inspired approach. *Chem - A Eur J* 20(25):7776. <https://doi.org/10.1002/chem.201402241>
- [61] Mahiya S, Lofrano G, Sharma SK (2014) Heavy metals in water, their adverse health effects and Biosorptive removal: A review. *Int J Chem* 3:132–149 ISSN: 2249 -2119
- [62] Cortes MT, Blanco D, Quinchaneque I (2019) Bioinspired polydopamine synthesis and its electrochemical characterization. *J Chem Educ* 96:1250. <https://doi.org/10.1021/acs.jchemed.8b00432>
- [63] Wang D, Wang Q, Lin Z, Pang T, Ding N (2023) Effect of pH and concentration of dopamine solution on the deposited polydopamine film and the prepared. *Crystals* 13:607
- [64] Gong H, Freudenberg N, Nie M et al (2016) BiVO<sub>4</sub> photoanodes for water splitting with high injection efficiency, deposited by reactive magnetron co-sputtering. *AIP Adv* 6:045108. <https://doi.org/10.1063/1.4947121>
- [65] Salaman J, Sathishkumar Y, Ramachandran K et al (2015) One-pot synthesis of magnetite nanorods/graphene composites and its catalytic activity toward electrochemical detection of dopamine. *Biosens Bioelectron* 64:269–276. <https://doi.org/10.1016/j.bios.2014.08.085>
- [66] Zangmeister RA, Morris TA, Tarlov MJ (2013) Characterization of polydopamine thin films deposited at short times by autoxidation of dopamine. *Langmuir* 29:8619. <https://doi.org/10.1021/la400587j>
- [67] Batul R, Bhawe M, Mahon PJ, Yu A (2020) Polydopamine nanosphere with in-situ loaded gentamicin and its antimicrobial activity. *Molecules* 25:2090. <https://doi.org/10.3390/molecules25092090>
- [68] Gong S, Xiao X, Sam DK et al (2019) Dispersed copper nanoparticles promote the electron mobility of nitrogen-rich graphitized carbon aerogel for electrochemical determination of 4-nitrophenol. *Microchim Acta* 186:853. <https://doi.org/10.1007/s00604-019-3841-7>
- [69] Wawrzyniak J, Karczewski J, Coy E et al (2021) Spectacular oxygen evolution reaction enhancement through laser processing of the nickel-decorated titania nanotubes. *Adv Mater Interfaces* 8:1–6. <https://doi.org/10.1002/admi.202001420>
- [70] Xiong D, Liu L, Li W (2017) Vertically aligned porous nickel(II) hydroxide nanosheets supported on carbon paper with long-term oxygen evolution performance. *Chem - An Asian J* 12:543–551. <https://doi.org/10.1002/asia.201601590>
- [71] Cheng H, Liu Y, Li X et al (2021) Efficient recovery of Cr(vi) from electroplating wastewater by iron-modified sludge-based hollow-structured porous carbon: coexistence effects and competition for adsorption. *RSC Adv* 11:37233–37245. <https://doi.org/10.1039/d1ra06969a>
- [72] (2004) CRC Handbook of Chemistry and Physics, 84th Edition Edited by David R. Lide (National Institute of Standards and Technology). *J Am Chem Soc* 126:1586. <https://doi.org/10.1021/ja0336372>
- [73] Boubatra M, Azizi A, Schmerber G (2012) The influence of pH electrolyte on the electrochemical deposition and properties of nickel thin films. *Ionics (Kiel)* 18:425–432. <https://doi.org/10.1007/s11581-011-0642-3>
- [74] Fan Z, Ding B, Guo H et al (2019) Dual dopamine derived polydopamine coated N-doped porous carbon spheres as a sulfur host for high-performance lithium–sulfur batteries. *Chem - A Eur J* 25(45):10710. <https://doi.org/10.1002/chem.201901591>

- [75] Bharathi K, Kumar SP, Prasab PS et al (2017) Voltammetric sensing of dopamine at a glassy carbon electrode modified with III, Chromium Base. *Schiff. Mech Mater Sci Eng*. <https://doi.org/10.2412/mmse.66.65.502>
- [76] Kita E, Chatlas J, Szabłowicz M (2003) Kinetics and mechanism of one dipicolinato ligand substitution in the chromium ( III )–bis ( dipicolinato ) complex : an unusual rate dependence on acid concentration. *Transit Met Chem* 28:9–15. <https://doi.org/10.1023/A:1022535803814>
- [77] Lipińska W, Grochowska K, Karczewski J et al (2020) Thermally tuneable optical and electrochemical properties of Au-Cu nanomosaic formed over the host titanium dimples. *Chem Eng J*. <https://doi.org/10.1016/j.cej.2020.125673>
- [78] Seenivasan H, Bera P, Balaraju JN, Rajam KS (2013) XPS characterization and microhardness of heat treated Co–W coatings electrodeposited with gluconate bath. *Adv Sci Focus* 1:262–268. <https://doi.org/10.1166/asfo.2013.1033>
- [79] Song KH, Jeong SK, Jeong BH, Lee K (2020) Acid/base-treated activated carbon catalysts for the low-temperature endothermic cracking of N -dodecane with applications in hypersonic vehicle heat management system. *Catalysts* 10:1149. <https://doi.org/10.3390/catal10101149>
- [80] Simpson R, White RG, Watts JF, Baker MA (2017) XPS investigation of monatomic and cluster argon ion sputtering of tantalum pentoxide. *Appl Surf Sci* 405:79–87. <https://doi.org/10.1016/j.apsusc.2017.02.006>
- [81] Ryvkin F, Greenaway FT (2010) Modeling Cu(II) binding to peptides using the extensible systematic force field. *Bioinorg Chem Appl* 2010:724210. <https://doi.org/10.1155/2010/724210>
- [82] Vaughn BA, Brown AM, Ahn SH et al (2020) Is less more? Influence of the coordination geometry of copper(II) picolinate chelate complexes on metabolic stability. *Inorg Chem* 59:16095–16108. <https://doi.org/10.1021/acs.inorgchem.0c02314>
- [83] Monti S, Corozzi A, Fristrup P et al (2013) Exploring the conformational and reactive dynamics of biomolecules in solution using an extended version of the glycine reactive force field. *Phys Chem Chem Phys* 15:15062–15077. <https://doi.org/10.1039/C3CP51931G>
- [84] Hardcastle FD (2011) Raman spectroscopy of Titania (TiO<sub>2</sub>) nanotubular water-splitting catalysts. *J Ark Acad Sci* 65:43–48
- [85] Ma JX, Yang H, Ren R et al (2015) Well-dispersive graphene-polydopamine-Pd hybrid with enhanced catalytic performance. *RSC Adv* 5:97520–97527. <https://doi.org/10.1039/C5RA13361K>
- [86] Huang R, Zhang Y, Zhang Z et al (2022) Design of flexible film-forming polydopamine / polypyrrole / nanodiamond hierarchical structure for broadband microwave absorption. *Polymers (Basel)* 14:2014. <https://doi.org/10.3390/polym14102014>
- [87] Yang P, Wang Z (2020) Recent developments in polydopamine fluorescent nanomaterials. *Mater Horizons* 7:746–761. <https://doi.org/10.1039/c9mh01197h>
- [88] Koh DY, Kook JK, Lee SW (2020) Highly fluorescent oligodopamine ( F-ODA ) for accurate and sensitive detection of the neurotransmitter dopamine. *Anal Biochem* 591:113571. <https://doi.org/10.1016/j.ab.2019.113571>
- [89] Qin Y, Li Y, Tian Z et al (2016) Efficiently visible-light driven photoelectrocatalytic oxidation of as(III) at low positive biasing using Pt/TiO<sub>2</sub> nanotube electrode. *Nanoscale Res Lett* 11:32. <https://doi.org/10.1186/s11671-016-1248-5>
- [90] Xuwen H, Feng T, Zhaoxia J (2018) Free-standing polydopamine films generated in the presence of different metallic ions: the comparison of reaction process and film properties. *RCS Adv* 8:18347–18354. <https://doi.org/10.1039/C8RA02930J>
- [91] Barreto WJ, Ando A, Santos PS, et al. (2008) *Spectrochimica Acta Part A: Molecular and Biomolecular Spectroscopy* Raman, IR, UV – vis and EPR characterization of two copper dioxolene complexes derived from L-dopa and dopamine. 71:1419–1424. <https://doi.org/10.1016/j.saa.2008.04.014>
- [92] Barreto WJ, Stucchi F (2007) A Spectroscopic and Kinetic Investigation on the Substitution of Fe ( III ) for Ni ( II ) in a Siderophore Model. *Zeitschrift für Naturforsch B* 62:685–690. <https://doi.org/10.1515/znb-2007-0510>
- [93] Reynal A, Willkomm J, Muresan NM et al (2014) Distance dependent charge separation and recombination in semiconductor/molecular catalyst systems for water splitting. *Chem Commun* 50:12768–12771. <https://doi.org/10.1039/c4cc05143b>
- [94] Wu M, Jing T, Tian J et al (2022) Synergistic effect of silver plasmon resonance and p-n heterojunction enhanced photoelectrochemical aptasensing platform for detecting chloramphenicol. *Adv Compos Hybrid Mater* 5:2247–2259. <https://doi.org/10.1007/s42114-021-00377-z>
- [95] Nakayama M, Suzuki K, Fujii K (2019) Single-ion catalyst of Ni<sup>2+</sup> anchored in the interlayer space of layered MnO<sub>2</sub> for electro-oxidation of ethanol in alkaline electrolyte. *Electrochem Commun* 105:106492. <https://doi.org/10.1016/j.elecom.2019.106492>
- [96] Terna AD, Elemike EE, Mbonu JI et al (2021) The future of semiconductors nanoparticles: Synthesis, properties and applications. *Mater Sci Eng B* 272:115363. <https://doi.org/10.1016/j.mseb.2021.115363>
- [97] Paulus GLC, Ham M, Strano MS (2012) Anomalous thickness-dependence of photocurrent explained for state-of-the-art planar nano-heterojunction organic solar cells. *Nanotechnology* 23:095402. <https://doi.org/10.1088/0957-4484/23/9/095402>
- [98] Pisarek M, Krawczyk M, Kosiński A et al (2021) Materials characterization of TiO<sub>2</sub> nanotubes decorated by Au nanoparticles for photoelectrochemical applications. *RSC Adv* 11:38727–38738. <https://doi.org/10.1039/d1ra07443a>
- [99] Mortazavi B, Javvaji B, Shojaei F et al (2021) Exceptional piezoelectricity, high thermal conductivity and stiffness and promising photocatalysis in two-dimensional MoSi<sub>2</sub>N<sub>4</sub> family confirmed by first-principles. *Nano Energy* 82:105716. <https://doi.org/10.1016/j.nanoen.2020.105716>
- [100] Mortazavi B, Silani M, Podryabinkin EV et al (2021) First-principles multiscale modeling of mechanical properties in graphene/borophene heterostructures empowered by machine-learning interatomic potentials. *Adv Mater* 33:2102807. <https://doi.org/10.1002/adma.202102807>

**Publisher's Note** Springer Nature remains neutral with regard to jurisdictional claims in published maps and institutional affiliations.